J. Fluid Mech. (2013), *vol.* 727, *pp.* 582–611.
doi:10.1017/jfm.2013.279

Drops bouncing on a vibrating bath

Jan Moláček and John W. M. Bush†

Department of Mathematics, Massachusetts Institute of Technology, 77 Massachusetts Avenue, Cambridge, MA 02139, USA

(Received 7 December 2012; revised 1 April 2013; accepted 24 May 2013)

We present the results of a combined experimental and theoretical investigation of millimetric droplets bouncing on a vertically vibrating fluid bath. We first characterize the system experimentally, deducing the dependence of the droplet dynamics on the system parameters, specifically the drop size, driving acceleration and driving frequency. As the driving acceleration is increased, depending on drop size, we observe the transition from coalescing to vibrating or bouncing states, then period-doubling events that may culminate in either walking drops or chaotic bouncing states. The drop's vertical dynamics depends critically on the ratio of the forcing frequency to the drop's natural oscillation frequency. For example, when the data describing the coalescence–bouncing threshold and period-doubling thresholds are described in terms of this ratio, they collapse onto a single curve. We observe and rationalize the coexistence of two non-coalescing states, bouncing and vibrating, for identical system parameters. In the former state, the contact time is prescribed by the drop dynamics; in the latter, by the driving frequency. The bouncing states are described by theoretical models of increasing complexity whose predictions are tested against experimental data. We first model the drop–bath interaction in terms of a linear spring, then develop a logarithmic spring model that better captures the drop dynamics over a wider range of parameter space. While the linear spring model provides a faster, less accurate option, the logarithmic spring model is found to be more accurate and consistent with all existing data.

Key words: drops, Faraday waves, waves/free-surface flows

1. Introduction

The impact of a liquid drop on a quiescent liquid bath has been widely studied due to its visual appeal and its importance in both natural processes and industrial applications (Schotland 1960; Jayaratne & Mason 1964; Ching, Golay & Johnson 1984; Hallett & Christensen 1984; Cai 1989; Prosperetti & Oguz 1993). While relatively straightforward to study experimentally since the advent of the high-speed video camera, drop impact remains a challenging problem to treat analytically or to simulate numerically. We here consider relatively low-energy impacts, in which the droplet may rebound cleanly from the surface after a collision in which both the droplet and bath are only weakly distorted.

† Email address for correspondence: bush@math.mit.edu

Symbol	Meaning	Typical value
R_0	Drop radius	0.07–0.8 mm
ρ	Silicone oil density	949–960 kg m^{-3}
ρ_a	Air density	1.2 kg m^{-3}
σ	Drop surface tension	20–21 mN m^{-1}
g	Gravitational acceleration	9.81 m s^{-2}
V_{in}	Drop incoming speed	0.1–1 m s^{-1}
V_{out}	Drop outgoing speed	0.01–1 m s^{-1}
μ	Drop dynamic viscosity	10^{-3}–10^{-1} kg m^{-1} s^{-1}
μ_a	Air dynamic viscosity	1.84×10^{-5} kg m^{-1} s^{-1}
ν	Drop kinematic viscosity	10–100 cSt
ν_a	Air kinematic viscosity	15 cSt
T_C	Contact time	1–20 ms
C_R	$= V_{in}/V_{out}$ Coefficient of restitution	0–0.4
f	Bath shaking frequency	40–200 Hz
ω	$= 2\pi f$ Bath angular frequency	250–1250 rad s^{-1}
γ	Peak bath acceleration	0–70 m s^{-2}
ω_D	$= (\sigma/\rho R_0^3)^{1/2}$ Characteristic drop oscillation frequency	300–5000 s^{-1}
We	$= \rho R_0 V_{in}^2/\sigma$ Weber number	0.01–1
Bo	$= \rho g R_0^2/\sigma$ Bond number	10^{-3}–0.4
Oh	$= \mu(\sigma\rho R_0)^{-1/2}$ Drop Ohnesorge number	0.004–2
Oh_a	$= \mu_a(\sigma\rho R_0)^{-1/2}$ Air Ohnesorge number	10^{-4}–10^{-3}
Ω	$= 2\pi f\sqrt{\rho R_0^3/\sigma}$ Vibration number	0–1.4
Γ	$= \gamma/g$ Peak non-dimensional bath acceleration	0–7

TABLE 1. List of symbols used together with typical values encountered in our experiments, as well as those reported by Protière *et al.* (2006) and Eddi *et al.* (2011*b*).

The dynamics of the drop impact depends in general on the drop inertia, surface tension, viscous forces within the drop, bath and surrounding air, and gravity. Restricting attention to the case of a drop's normal impact on a quiescent bath of the same liquid reduces the number of relevant physical variables to six: the gravitational acceleration g, the droplet radius R_0 and impact speed V_{in}, the liquid density ρ, dynamic viscosity μ and surface tension σ (see table 1). These give rise to three dimensionless groups: the Weber number $We = \rho R_0 V_{in}^2/\sigma$, Bond number $Bo = \rho g R_0^2/\sigma$ and Ohnesorge number $Oh = \mu(\sigma\rho R_0)^{-1/2}$ prescribe the relative magnitudes of, respectively, inertial and gravitational pressure and viscous stresses to curvature pressures associated with surface tension (see table 1 for a summary of our notation). Considering the effects of the surrounding gas on the drop dynamics requires the inclusion of two more physical variables, the gas density ρ_g and gas viscosity μ_g, which require in turn two additional dimensionless groups, ρ_g/ρ and $Oh_g = \mu_g(\sigma\rho R_0)^{-1/2}$. For the parameter ranges of interest in our study, $\rho_g/\rho \ll 1$ and $Oh_g \ll Oh$. Thus, beyond providing the lubrication layer between drop and bath that allows the bouncing states, the influence of air on the dynamics is negligible. When the bath is shaken vertically, two additional parameters enter into the dynamics, the frequency f and peak acceleration γ of the bath vibration. These give rise to two new dimensionless groups, the first being the dimensionless bath acceleration $\Gamma = \gamma/g$, and the second being the ratio of the driving angular frequency $\omega = 2\pi f$ to the

characteristic drop oscillation frequency $\omega_D = (\sigma/\rho R_0^3)^{1/2}$ (Rayleigh 1879). We call this ratio the vibration number $\Omega = \omega/\omega_D$.

At low forcing amplitude, the drop comes to rest on the vibrating bath, oscillating with the driving frequency while the air layer drains beneath it. Once the thickness decreases below the range of molecular forces, the two interfaces connect and the drop is absorbed into the bath. When the driving acceleration reaches a value corresponding to the bouncing threshold, the bath can transfer enough momentum during impact to compensate for the energy lost; consequently, the drop can be sustained indefinitely in a periodic bouncing motion (Walker 1978). In this bouncing regime, the drop and the bath never come into contact, which would lead to coalescence; instead, they remain separated by an air layer that is replenished after each collision (Couder *et al.* 2005*a*). We note that there is also a strict upper bound on the bath acceleration that will permit stable bouncing states: beyond a critical value γ_F, known as the Faraday threshold, the entire bath surface becomes unstable to a standing field of Faraday waves with frequency $f/2$ (Faraday 1831; Benjamin & Ursell 1954). For a theory describing the dependence of the Faraday threshold on viscosity, see Kumar (1996). All experiments reported here were performed below the Faraday threshold.

As the amplitude of the bath oscillation is increased beyond the bouncing threshold, the drop's periodic bouncing may become unstable and undergo a period-doubling cascade leading to a chaotic vertical motion, a feature common to systems involving bouncing on vibrating substrates. The most commonly studied scenario, first proposed by Fermi (1949) as a model of cosmic rays, is the dynamics of a ball bouncing on a vibrating rigid surface (Pieranski 1983; Pieranski & Bartolino 1985; Everson 1986; Luna-Acosta 1990; Davis & Virgin 2007). The dynamics of a drop bouncing on a highly viscous liquid bath has been examined by Terwagne *et al.* (2008), and that of a rigid ball bouncing on a vibrated elastic membrane by Eichwald *et al.* (2010). Gilet & Bush (2009*a*,*b*) examined the dynamics of a liquid drop bouncing on a soap film and noted the coexistence of multiple bouncing states for a given set of system parameters, an effect that arises also in our system.

For drops within a certain size range, the interplay between the drop and the waves it excites on the liquid surface causes the vertical bouncing to become unstable; as a result, the drop begins to move horizontally, an effect first reported by Couder *et al.* (2005*b*). As the bath acceleration approaches the Faraday threshold from below, the decay rate of the surface waves created by the drop impacts is reduced and a particular wavelength is selected, corresponding to the most unstable Faraday wavenumber. Interaction of walking drops and the surface waves reflected from the boundaries (Couder & Fort 2006; Eddi *et al.* 2009*b*) or from other drops (Protière *et al.* 2005; Protière, Boudaoud & Couder 2006; Protière & Couder 2006; Protière, Bohn & Couder 2008; Eddi *et al.* 2009*a*; Fort *et al.* 2010; Eddi, Boudaoud & Couder 2011*a*; Eddi *et al.* 2011*b*) leads to a variety of interesting phenomena reminiscent of quantum mechanics (Bush 2010). Examples include tunnelling across a subsurface barrier (Eddi *et al.* 2009*b*), single-particle diffraction in both single- and double-slit geometries (Couder & Fort 2006), quantized orbits analogous to Landau levels in quantum mechanics (Fort *et al.* 2010) and orbital level splitting (Eddi *et al.* 2012). Harris *et al.* (2013) considered a drop walking in confined geometries, and demonstrated that the resulting probability distribution function is simply related to the most unstable Faraday wave mode of the cavity. Rationalizing these remarkable macroscopic quantum-like phenomena provided the motivation for this study. In a companion paper, we focus on the dynamics of the walking drops (Moláček & Bush 2013, henceforth MBII). Our studies will make clear that, in order to understand the

role of drop size and driving frequency on the horizontal dynamics, a model of both the vertical and horizontal drop motion is required. The former will be developed herein.

Gilet & Bush (2009*b*) demonstrated that, for the case of a drop bouncing on a soap film, the surface energy of the film increases quadratically with the drop's penetration depth, and thus the film's effect on the drop is analogous to that of a linear spring with a spring constant proportional to the surface tension. When a drop impacts a rigid surface, one can approximate the drop's shape by its first two spherical harmonics, leading to a linear dependence of reaction force on the deformation amplitude and of the viscous drag on the speed of the drop's centre of mass (Okumura *et al.* 2003). Thus, the interactions in these two disparate systems can both be modelled in terms of a damped linear spring. To model drop impact on a liquid bath, Terwagne (2011) augmented the model of Okumura *et al.* (2003) by adding a second spring that captures the role of surface energy stored in the bath deformation. Such linear spring models break down when the inertial stresses become comparable to the surface tension ($We \gtrsim 1$), or when the surface deformation ceases to be small relative to the drop radius. The range of Weber numbers encountered in the current study extends beyond 1, motivating the introduction of a more complex model.

Protière *et al.* (2006) were the first to publish a regime diagram indicating the behaviour of liquid drops bouncing on a liquid bath (specifically, 20 cSt silicone oil), followed by Eddi *et al.* (2008), who used 50 cSt oil. We here extend their measurements, covering a wider range of drop size and driving frequencies, in order to have a firmer experimental basis for building our theoretical model of the drop dynamics. The goal of this paper is to rationalize the regime diagrams for the vertical motion of the bouncing drops, such as that shown in figure 3. In addition to providing a consistent means by which to describe the vertical dynamics, the model presented here will provide a crucial prerequisite to rationalizing the drop's horizontal motion, which will be the subject of a companion paper (MBII).

In § 2 we describe our experimental arrangement and present our data on the transitions between different vertical bouncing states. In § 3 we develop a theoretical description of the vertical dynamics of drops bouncing on a vertically vibrated bath. We first consider a linear spring model, and examine its range of validity and shortcomings, which motivate the development of a 'logarithmic spring' model in § 3.2. The logarithmic spring model best rationalizes the experimentally measured regime diagrams; moreover, it reproduces the observed dependence of the coefficient of restitution and contact time on the Weber number. Finally, future directions are outlined in § 4.

2. Experiments

In order to extend the datasets reported by Protière *et al.* (2006) and Eddi *et al.* (2008), we have recorded the behaviour of droplets of silicone oil of viscosity 20 and 50 cSt over a wide range of drop sizes and driving frequencies. A schematic illustration of the experimental apparatus is shown in figure 1. A liquid drop of undeformed radius R_0 bounces on a bath of the same liquid (figure 2), in our case silicone oil with density $\rho = 949$ kg m^{-3}, surface tension $\sigma = 20.6 \times 10^{-3}$ N m^{-1} and kinematic viscosity $\nu = 20$ cSt, or a more viscous silicone oil with $\rho = 960$ kg m^{-3}, $\sigma = 20.8 \times 10^{-3}$ N m^{-1} and $\nu = 50$ cSt. The bath, of depth $h_B \approx 9$ mm, is enclosed in a cylindrical container with diameter $D = 76$ mm. The container is shaken vertically,

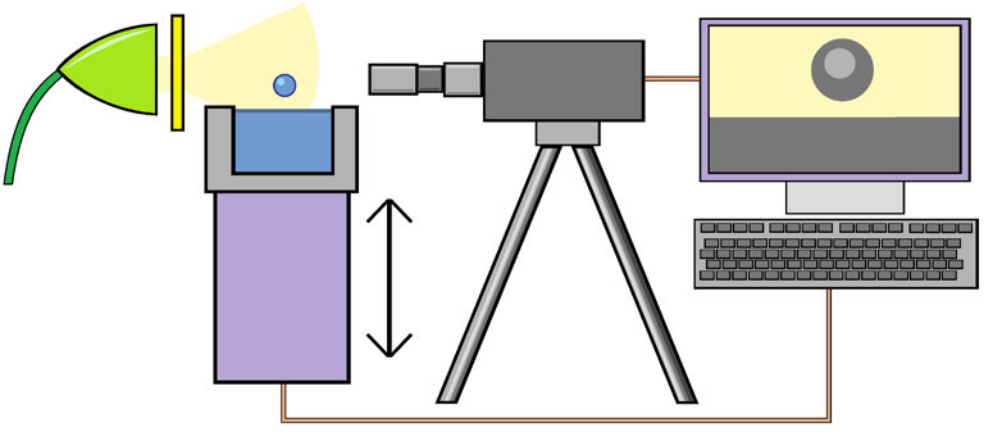

FIGURE 1. (Colour online) A schematic illustration of the experimental set-up. A liquid drop bounces on a liquid bath enclosed in a circular container shaken vertically. The drop is illuminated by a strong light-emitting diode lamp through a diffuser, and its motion recorded by a high-speed camera that can be synchronized with the shaker.

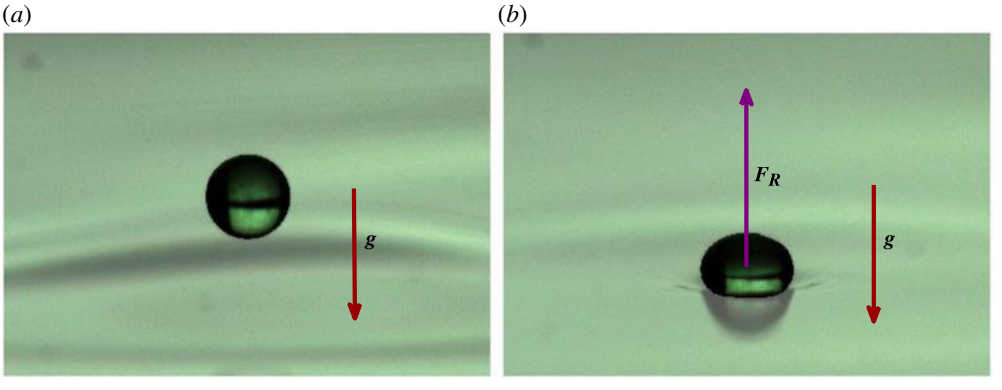

FIGURE 2. (Colour online) A droplet of radius $R_0 = 0.38$ mm (*a*) in flight and (*b*) during contact with the bath. The drop motion is determined by the gravitational force $\boldsymbol{g}$ and the reaction force $\boldsymbol{F_R}$ generated during impact.

sinusoidally in time, with peak acceleration γ and frequency f, so that the effective gravity in the bath frame of reference is $g + \gamma \sin(2\pi ft)$.

The motion of the drop was observed using a high-speed camera synchronized with the shaker. The camera resolution is 86 pixel mm^{-1} and the distance of the drop from the camera was controlled with approximately 1 % error by keeping the drop in focus, giving a total error in our drop radius measurement of less than 0.01 mm. The drops were created by dipping a needle in the bath followed by its fast retraction. In order to systematically sweep the range of drop radii, we started with a drop at the lower end of the spectrum (radius of roughly 0.1 mm), and repeatedly enlarged it by merging it with other small drops. We limit ourselves to the range 0.07 mm $< R_0 <$ 0.8 mm, since larger drops do not exhibit any novel behaviour, while smaller drops tend to coalesce for the range of driving accelerations considered ($0 < \gamma < 7g$). The notation adopted in this paper together with the range of physical variables considered are defined in table 1.

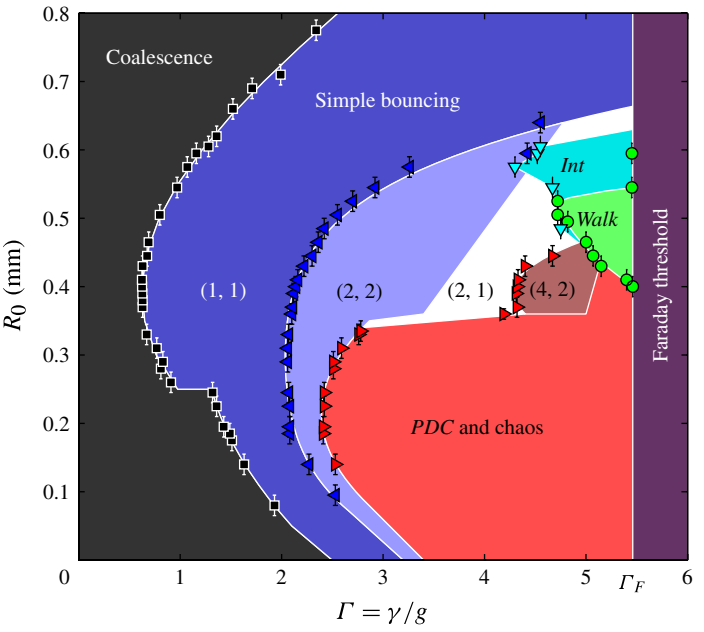

FIGURE 3. (Colour online) Regime diagram describing the motion of a silicone oil droplet of viscosity 50 cSt on a bath of the same fluid vibrating with frequency 60 Hz. The horizontal axis is the dimensionless peak acceleration of the bath $\Gamma = \gamma/g$, while the vertical axis is the drop radius. The bath surface becomes unstable when Γ exceeds the Faraday threshold $\Gamma_F = 5.46$ (vertical line). Only the major dynamical regimes are shown: *PDC* signifies the period-doubling cascade, *Int* the region of intermittent horizontal movement, and *Walk* the walking regime. Lines indicate best fits to threshold curves.

2.1. *Regime diagrams*

A typical regime diagram is shown in figure 3, where we adopt the nomenclature used by Protière *et al.* (2006). For a droplet of fixed size, below a certain driving acceleration γ_B, the vibrating bath is unable to compensate for the drop's loss of mechanical energy during impact, and the droplet coalesces after a series of increasingly small jumps. For $\gamma > \gamma_B$, the drop bounces with the same period as that of the bath. When the driving acceleration is further increased, small drops (with $\Omega \lesssim 0.6$) undergo a period-doubling cascade (denoted *PDC* in the figure) that culminates in a chaotic region. Note that the finite (non-zero) duration of contact between the drop and the bath precludes the existence of the locking regions described by Luck & Mehta (1993). As the driving amplitude is increased further, one observes chaotic regions interspersed with islands of periodicity, most significant for our purposes being the region where the drop bounces with twice the driving period. It is in this regime that the bouncers achieve resonance with their Faraday wave field and so transform into walkers.

Compared to the previously published regime diagrams (Protière *et al.* 2006; Eddi *et al.* 2008), our data offer the first insight into the behaviour of the threshold curves for small drop sizes. The bouncing and period-doubling threshold curves are not nearly vertical for small drops, as previously suggested, but in fact curve towards higher values of Γ as $R_0 \to 0$. Other novel features are the discontinuity of the bouncing

threshold curve at $R_0 = 0.25$ mm and the realization that the region between the first and second period-doubling transitions contains both the $(2, 2)$ and the $(2, 1)$ modes.

Following Gilet & Bush (2009*b*), we adopt the (m, n) notation to distinguish between different bouncing modes. In the (m, n) mode, the drop's vertical motion has period equal to m driving periods, and within this period the drop contacts the bath n times. By *contact* we refer to that part of the drop's motion when the drop and bath are being deformed and the air pressure beneath the drop is significantly elevated above that of the ambient air. We stress that the drop and the bath always remain separated by an intervening air layer and thus never actually come into contact. Provided the rebound time is shorter than the time required for the intervening layer to thin below a certain critical thickness, the drop will detach without coalescing. The chaotic region is thus difficult to observe experimentally for small drops (i.e. $\Omega \lesssim 0.6$): once the bouncing becomes chaotic, the drop will eventually undergo a chattering sequence and coalesce.

An interesting feature of the system is that there can be more than one stable bouncing mode for a given combination of drop size and driving (Terwagne *et al.* 2013). Indeed, several stable periodic motions may coexist, corresponding to the same mode (m, n) but having different average mechanical energy (see figures 4, 16 and 17) and average contact time. In order to distinguish between different bouncing states with the same mode number (m, n), we denote them by $(m, n)^p$. Thus $(m, n)^1$ signifies the motion with the least average energy (corresponding usually to the longest average contact time) and the p index increases with increasing average energy. Larger drops do not undergo a full period-doubling cascade (refer to figure 3): after transitioning from the $(1, 1)$ mode to the $(2, 2)$ mode, further increase of γ leads to increasing disparity between the large and small jumps, until the smaller jump disappears completely. Thus the drop transitions from the $(2, 2)$ mode into the $(2, 1)$ mode. This mode then undergoes a period-doubling cascade and only then enters a chaotic regime. Near the Faraday threshold (as occurs at $\Gamma = 5.46$ for 50 cSt oil at $f = 60$ Hz), the interaction between the drop and the slowly decaying standing waves created by its previous impacts may lead either to walking or to an intermittent behaviour (denoted *Int* in figure 3), where the drop performs a complicated aperiodic horizontal motion and does not settle into a steady walking state.

In figure 4, we show the vertical motion of 50 cSt silicone oil droplets for several driving accelerations over the course of five driving periods. We show the five most prevalent modes, specifically the $(1, 1)^1$, $(1, 1)^2$, $(2, 2)$, $(2, 1)^1$ and $(2, 1)^2$ modes, that emerge as the driving acceleration is increased progressively. Note that the amplitude of the drop's motion increases with driving acceleration. The motion of the bath surface cannot be directly observed in figure 4 due to the nature of the illumination; nevertheless, one can determine the contact time from the relative positions of the drop and its reflection in the bath.

We measured the bouncing threshold and the first two period-doubling thresholds of silicone oil droplets with $\nu = 20$ cSt and $40\ \text{Hz} \leqslant f \leqslant 200$ Hz, and with $\nu = 50$ cSt and $60\ \text{Hz} \leqslant f \leqslant 100$ Hz. The results are shown in figures 5–8. In figure 5, the bouncing threshold $\Gamma_B = \gamma_B(R_0, f, \nu)/g$, the minimum driving acceleration needed to prevent the drop from coalescing, is shown as a function of the drop size (vertical axis). We observe that the size of the drop that attains a bouncing state at the lowest Γ decreases with increasing frequency, while the minimum of Γ_B remains roughly constant. One expects that the minimum of Γ_B corresponds to the drop size for which the driving frequency equals the resonant frequency of the drop–bath system, with a shift due to the effects of viscosity. Using the vibration number $\Omega = \omega/\omega_D$ instead of

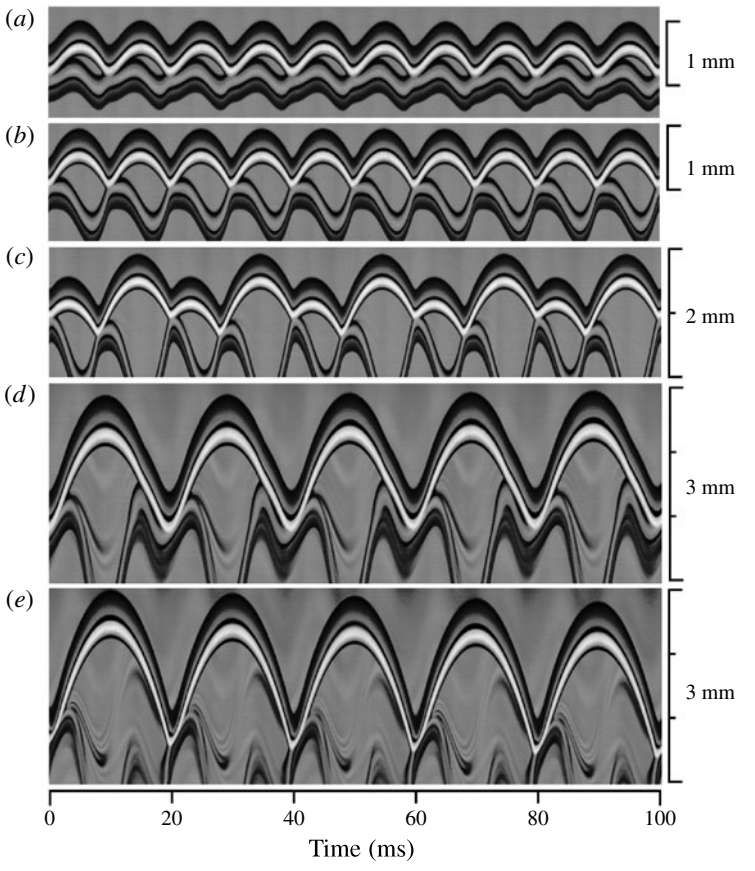

FIGURE 4. The simplest modes of vertical motion for 50 cSt silicone oil drops bouncing on a liquid bath vibrating with frequency 50 Hz. These are, in order of increasing dimensionless forcing $\Gamma = \gamma/g$: (*a*) the $(1, 1)^1$ mode, $\Gamma = 1.3$; (*b*) the $(1, 1)^2$ mode, $\Gamma = 1.4$; (*c*) the $(2, 2)^2$ mode, $\Gamma = 2.35$; (*d*) the $(2, 1)^1$ mode, $\Gamma = 3.6$; and (*e*) the $(2, 1)^2$ mode, $\Gamma = 4.1$. The drop radii are $R_0 = 0.28$ mm in panels (*a–c*) and $R_0 = 0.39$ mm in panels (*d*,*e*). The images were obtained by joining together vertical sections from successive video frames, each one 1 pixel wide and passing through the drop's centre. The camera was recording at 4000 frames per second. Note that in both the (2, 1) modes shown in panels (*d*,*e*) the drop was walking.

R_0 on the vertical axis, we see that the data for different frequencies nearly collapse onto a single curve (figure 6). Henceforth, we shall use Ω in order to display data for different frequencies in a single diagram.

In figure 6, we observe that the minimum of Γ_B occurs at $\Omega \approx 0.65$ for both viscosities, which corresponds to $R_0 \approx 0.47(\sigma/\rho f^2)^{1/3}$. We note that the minimum of Γ_B does depend weakly on the driving frequency (figure 6*b*). At higher frequencies, the typical drop radius near the minimum is smaller and the increasing influence of air drag and dissipation in the intervening air layer results in a shift of the bouncing threshold curve towards higher driving amplitudes (e.g. $f = 200$ Hz in figure 6). On the other hand, at lower frequencies, the typical drop radius near the minimum is larger and a relatively large portion of the mechanical energy is lost to the outgoing surface waves created by the drop motion. Thus there is an optimal frequency, in our

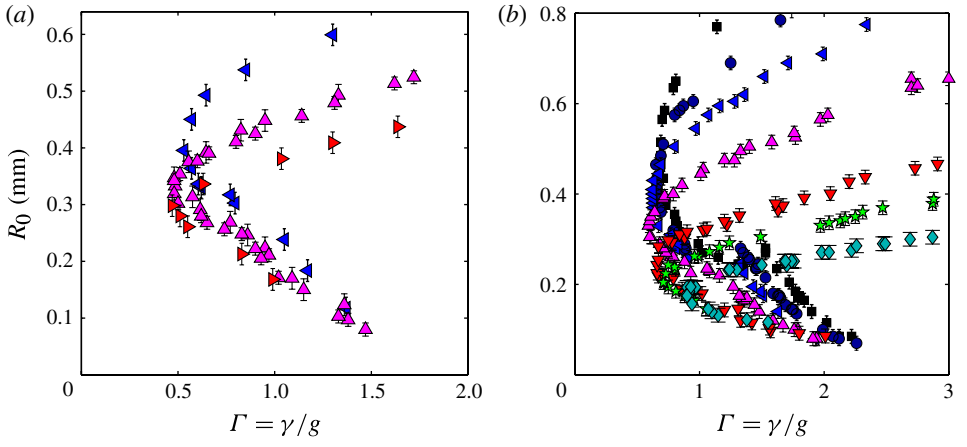

FIGURE 5. (Colour online) Bouncing thresholds measured for silicone oil droplets of viscosity (*a*) 20 cSt and (*b*) 50 cSt on a vibrating bath of the same oil. The minimum driving acceleration $\Gamma = \gamma/g$ (horizontal axis) required for sustained bouncing is shown as a function of the drop radius R_0 (vertical axis). Experimental results are shown for several driving frequencies f: 40 Hz (■), 50 Hz (●), 60 Hz (◀), 80 Hz (▲), 100 Hz (▶), 120 Hz (▼), 150 Hz (★) and 200 Hz (♦).

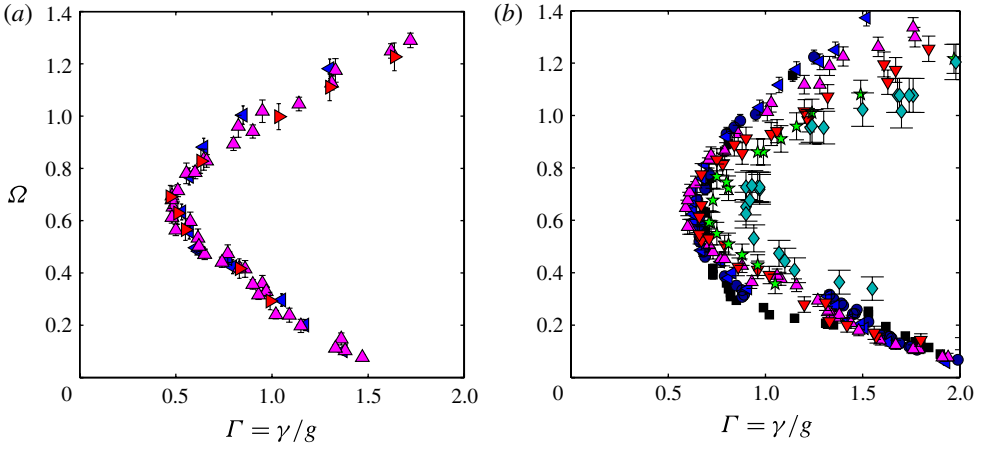

FIGURE 6. (Colour online) Bouncing thresholds. The same experimental data as shown in figure 5 is now plotted as a function of the vibration number $\Omega = \omega/\omega_D$ (vertical axis) instead of drop diameter R_0. Data for different frequencies collapse nearly onto a single curve.

case $f = 80$ Hz, for which the sum of these two effects is minimized and the global minimum of Γ_B is achieved. We observe $\Gamma_B \geqslant 0.47$ for $\nu = 20$ cSt and $\Gamma_B \geqslant 0.59$ for $\nu = 50$ cSt.

In figures 6(*b*) and 7, we see that the bouncing curves exhibit a discontinuity at approximately $\Omega = 0.2$–0.4. This discontinuity arises because smaller droplets can exist only in the higher-energy $(1, 1)^2$ mode and coalesce when this mode can no longer be sustained by the bath vibration. Larger drops can persist in the lower-energy $(1, 1)^1$ mode without coalescing because the intervening air layer takes a

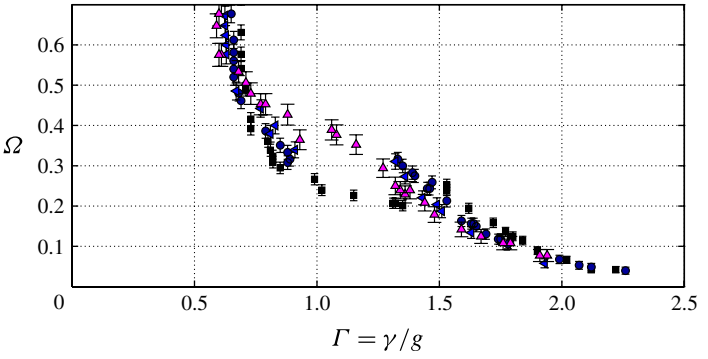

FIGURE 7. (Colour online) Detail of figure 6 showing the bouncing thresholds for silicone oil droplets of viscosity 50 cSt on a vibrating bath of the same oil. The minimum driving acceleration $\Gamma = \gamma/g$ (horizontal axis) needed to prevent the drop from coalescing with the bath is shown as a function of the vibration number $\Omega = \omega/\omega_D$ (vertical axis). Experimental results are shown for several driving frequencies f: 40 Hz (■), 50 Hz (●), 60 Hz (◀) and 80 Hz (▲). The discontinuity of the bouncing thresholds between $\Gamma = 1$ and $\Gamma = 1.2$ is clearly apparent.

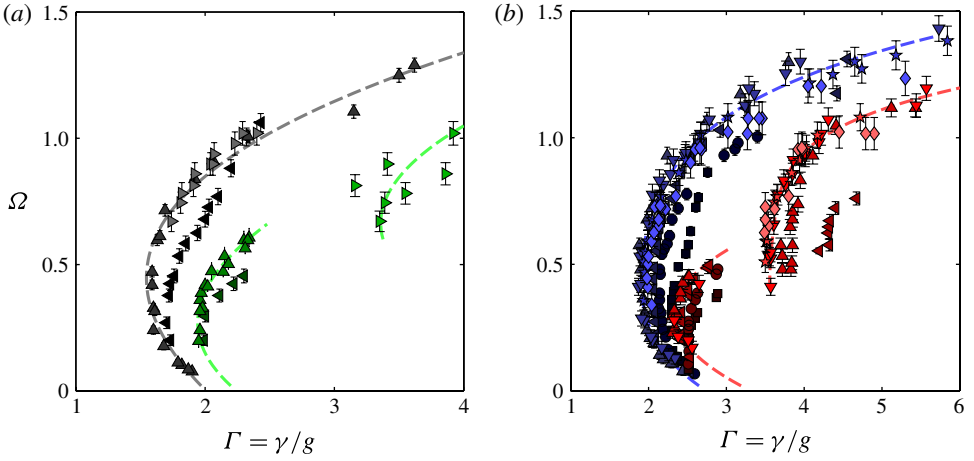

FIGURE 8. (Colour online) First two period-doubling thresholds for silicone oil droplets of viscosity (*a*) 20 cSt and (*b*) 50 cSt on a vibrating bath of the same oil. For smaller droplets ($\Omega < 0.6$) these are $(1, 1) \rightarrow (2, 2)$ and $(2, 2) \rightarrow (4, 4)$ transitions, while for larger drops ($\Omega > 0.6$) they are $(1, 1) \rightarrow (2, 2)$ and $(2, 1) \rightarrow (4, 2)$ transitions. The experimentally measured threshold acceleration $\Gamma = \gamma/g$ (horizontal axis) is shown as a function of the vibration number $\Omega = \omega/\omega_D$ (vertical axis) for several driving frequencies f: 40 Hz (■), 50 Hz (●), 60 Hz (◀), 80 Hz (▲), 100 Hz (▶), 120 Hz (▼), 150 Hz (⋆) and 200 Hz (⧫).

relatively long time to drain. Although determining the exact form of the bouncing threshold curve theoretically would require a detailed analysis of the intervening air layer dynamics (Hartland 1969, 1970; Jones & Wilson 1978), we will demonstrate in § 3 that the majority of the bouncing threshold curve runs along a mode threshold obtainable by relatively simple means.

Figure 8 shows the first two period-doubling thresholds. Smaller drops ($\Omega < 0.6$) undergo a period-doubling cascade, so the first two thresholds correspond to $(1,1) \to (2,2)$ and $(2,2) \to (4,4)$ transitions. Larger drops ($\Omega > 0.6$) transition from $(1,1)$ to $(2,2)$, then reduce the amplitude of their smaller bounce until a simple period-doubled bouncing mode $(2,1)$ is reached, and only then commence the period-doubling cascade $(2,1) \to (4,2) \to (8,4) \to \cdots$. Note that the low-frequency curves are shifted to the right of their high-frequency counterparts (60 Hz curve for 20 cSt; 50–60 Hz for 50 cSt), an effect due to the influence of the standing waves created on the bath by previous drop impacts. At lower frequencies, the Faraday threshold is closer to the period-doubling threshold; thus, the drop impacts create more slowly decaying standing waves on the bath surface. By reducing the relative speed between the drop and bath at impact, the standing waves appear to stabilize the vertical motion, and so delay the period-doubling transitions.

The bounds of the frequency range explored were prescribed by experimental constraints. The presence of the Faraday threshold provides a lower limit on the range of frequencies over which the period-doubled modes can arise. For example, for 20 cSt silicone oil, period-doubling occurs only for $\Gamma > 1.58$ (figure 8), while $\Gamma_F < 1.58$ for $f \leqslant 45$ Hz. Thus, for $f \leqslant 45$ Hz, the period-doubling transitions disappear. The upper limit on the frequency range is imposed by the finite resolution of our camera. Since the walking region of ultimate interest is given by $\Omega = 2\pi f\sqrt{\rho R_0^3/\sigma} \lesssim 1.5$ (see MBII), the typical size of a walker $R_0 \sim f^{-2/3}$. Thus, for higher frequencies, the constant error in drop size measurement leads to increasing relative error in Ω. Similarly, at high frequency, it becomes increasingly difficult to distinguish between the different bouncing modes, as the motion itself happens over a distance of at most $g(T/2)^2/2 \leqslant gf^{-2}/2$, which is of the order of 0.1 mm for $f = 200$ Hz.

3. Vertical dynamics

3.1. *Linear spring model*

We proceed by describing the simplest model of the drop's vertical dynamics, analogous to works by Okumura *et al.* (2003), Gilet & Bush (2009*b*) and Terwagne (2011), in which the drop–impactor interaction is described in terms of a linear spring. We non-dimensionalize the vertical displacement of the drop by its radius (see table 2 for a list of dimensionless variables) and time by the characteristic frequency of drop oscillations $\omega_D = \sqrt{\sigma/\rho R_0^3}$ (Rayleigh 1879). We shall always consider the frame of reference fixed relative to the shaking platform, and place the origin so that the undisturbed bath surface is at $Z = -1$ (see figure 9). Thus, a drop impacting an undisturbed surface will make a contact with the bath when its centre of mass is at $Z = 0$ and its base is at $Z = -1$. When the drop is not in contact with the bath ($Z > 0$), it is acted upon only by gravity (we neglect the air drag, an approximation to be justified later). Conversely, when it deforms the bath below its equilibrium height, we assume that the drop experiences an additional reaction force proportional to the penetration depth (CZ) and its energy is dissipated at a rate proportional to its speed relative to the bath ($D\,\partial Z/\partial\tau$ term). We thus expect the drop centre of mass $Z(\tau)$ to be governed by the following equation of motion:

$$\frac{\partial^2 Z}{\partial \tau^2} + H(-Z)\left(D\frac{\partial Z}{\partial \tau} + CZ\right) = -Bo^*(\tau). \tag{3.1}$$

Here $H(x)$ is the Heaviside step function, which indicates that the bath acts on the drop only when they are in contact; and $Bo^*(\tau) = Bo(1 + \Gamma \sin \Omega\tau)$ is the effective

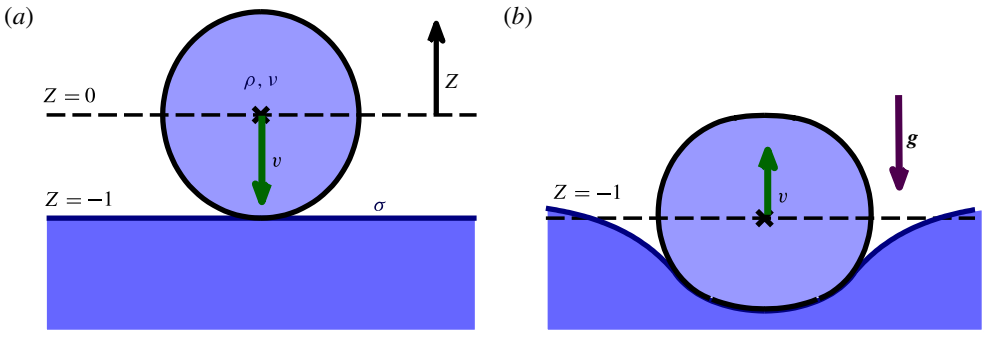

FIGURE 9. (Colour online) A schematic illustration of our choice of coordinates. (*a*) The vertical position of the drop's centre of mass Z is equal to 0 at the initiation of impact, and (*b*) would be -1 if it reached the equilibrium level of the bath.

Dimensional variable	Non-dimensional variable	Meaning
z	$Z = z/R_0$	Drop's vertical displacement
x	$X = x/R_0$	Drop's horizontal displacement
h	$H = h/R_0$	Bath distortion
t	$\tau = \omega_D t$	Time
T_C	$\tau_C = \omega_D T_C$	Dimensionless contact time
f	$\Omega = 2\pi f/\omega_D$	Vibration number

TABLE 2. List of variables used, along with their dimensionless counterparts. Here R_0 is the drop radius and $\omega_D = (\sigma/\rho R_0^3)^{1/2}$ is the characteristic drop oscillation frequency.

Bond number, which reflects the effective gravity in the vibrating bath frame of reference. The constants C and D can be determined from experiments by measuring, respectively, the coefficient of restitution C_R and the dimensionless contact time τ_C of the drop impacting a quiescent bath ($\Gamma = 0$). For small Bo ($Bo \ll Z_\tau(0)$), one can solve (3.1) over the duration of contact subject to the initial conditions $Z(0) = 0$ and $Z_\tau(0) = Z_{\tau 0}$ and so obtain $Z(\tau) \approx Z_{\tau 0} \exp(-D\tau/2) \sin(\sqrt{C'}\tau)/\sqrt{C'}$, where $C' = C - D^2/4$. Then we have the approximate relations $\tau_C = \pi/\sqrt{C'}$ and $C_R = \exp(-\pi D/2\sqrt{C'})$, or, conversely, $D = -2 \ln C_R/\tau_C$ and $C = (\pi^2 + \ln^2 C_R)/\tau_C^2$. As there is a one-to-one correspondence between pairs (C, D) and (C_R, τ_C), and the latter pair is easier to grasp intuitively, we shall henceforth use (C_R, τ_C) to characterize our linear spring model.

The crucial assumption underlying (3.1) is that, each time the drop strikes the vibrating bath, the disturbances created by its previous impacts have decayed sufficiently to be negligible. Similarly, it is assumed that any distortions and internal motions of the drop have decayed to the point where we can approximate the drop at impact as being spherical and in rigid-body motion. To check whether this assumption is reasonable for the range of parameters examined experimentally, we first look at the decay rate of drop oscillations. For small oscillations, this problem can be adequately described with a linear theory and has been treated in several classic papers

(Chandrasekhar 1961; Miller & Scriven 1968; Prosperetti 1980). The instantaneous drop shape can then be decomposed into spherical harmonics and the evolution of each mode treated separately by virtue of the linearity. It is found that the second harmonic mode (corresponding to ellipsoidal deformation) decays the slowest, and the rate of decay is equal to $3.8\mu/\rho R_0^2$ (Miller & Scriven 1968). Even if the oscillations are large and the linear theory is no longer accurate, we expect the deformations to decay at a comparable rate. The typical time between two subsequent excitations of the drop is given by $1/f$. Therefore, provided that $(\mu/\rho f R_0^2) > 0.5$, the oscillations will decay to less than $\exp(-19/10) \approx 0.15$ of their original magnitude and our assumption will be valid. This condition can be written in dimensionless form as

$$Oh > \frac{\Omega}{4\pi}. \tag{3.2}$$

Since we are interested only in the parameter regime for which $\Omega \lesssim 1.5$, we thus arrive at the condition $Oh > 0.12$. For silicone oil of viscosity 50 and 20 cSt, this is equivalent to requiring $R_0 < 8$ mm and $R_0 < 1.3$ mm, respectively, both of which are amply satisfied in our experiments.

When the driving amplitude is sufficiently far from the Faraday threshold, a similar argument can be made for the decay rate of the local bath deformation near the drop, composed of waves with wavelength comparable to or smaller than the drop radius. Note that each drop impact also creates a propagating wave on the bath, which decays relatively slowly due to its relatively long wavelength. We assume that this propagating wave is sufficiently far from the drop on its next impact that it has negligible influence on its dynamics. These inferences, that the drop returns to a spherical form and the local interface to a plane between impacts, are consistent with our observations, provided the system is sufficiently far from the Faraday threshold.

We now examine the region of validity of the second assumption used to derive (3.1), namely, that the influence of air drag on the vertical drop dynamics is negligible. When the drop is not in contact with the bath and $Re < 1$, approximating the air drag using the well-known Stokes formula for a rigid sphere gives

$$Z_{\tau\tau} = -Bo^*(\tau) - \tfrac{9}{2} Oh_a Z_\tau. \tag{3.3}$$

Here $Oh_a = \mu_a/\sqrt{\rho\sigma R_0}$ is the air Ohnesorge number, with μ_a being the dynamic viscosity of air. The Reynolds number is given by $Re = 2R_0 V/\nu_a = 2(|Z_\tau|/Oh_a)(\rho_a/\rho)$, with ν_a and ρ_a being the kinematic viscosity and density of the air. Since the maximum value of the Reynolds number during the bouncing motion is $Re_{max} \sim 2gR_0/f\nu_a$, we have $Re_{max} \sim 4$ for $f = 100$ Hz and $R_0 = 0.3$ mm, and $Re_{max} \sim 16$ for $f = 40$ Hz and $R_0 = 0.5$ mm. Therefore, the Stokes formula cannot be applied and we must use an approximation to the drag in the regime $1 < Re \leqslant 20$. A good approximation (accurate to within 10 % in the range $1 < Re < 50$) is given by (Flemmer & Banks 1986)

$$Z_{\tau\tau} = -Bo^*(\tau) - \tfrac{9}{2} Oh_a Z_\tau (1 + \tfrac{1}{12} Re). \tag{3.4}$$

Thus the air drag is negligible provided that $9Oh_a Z_\tau (1 + \frac{18}{12})/2 \ll Bo$. Since $Z_\tau \leqslant Bo(2\pi/\Omega)$ (acceleration multiplied by time), we arrive at the condition that

$$\frac{45\pi}{2} Oh_a \ll \Omega \quad \text{or} \quad \frac{\mu_a}{\rho R_0^2 f} \ll 0.09. \tag{3.5}$$

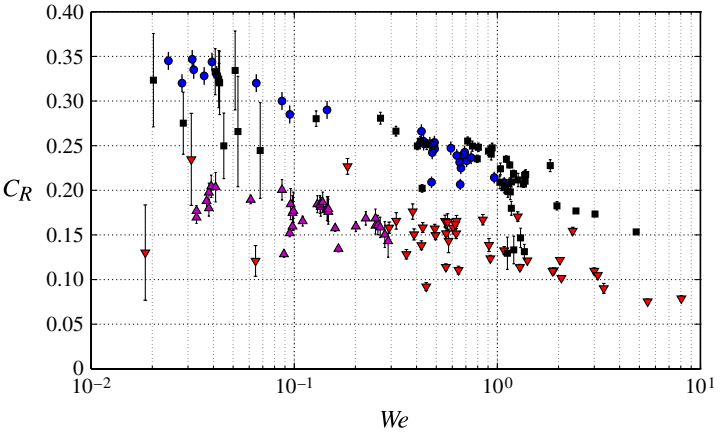

FIGURE 10. (Colour online) Normal coefficient of restitution $C_R = V_{out}/V_{in}$ of silicone oil droplets impacting a bath of the same liquid, as a function of the Weber number $We = \rho R_0 V_{in}^2/\sigma$. Shown are results for 20 cSt (■) and 50 cSt (▼) droplets impacting a quiescent bath, together with values measured from drops impacting a vibrating bath just above the bouncing threshold, for 20 cSt (●) and 50 cSt (▲), respectively.

As $R_0 \geqslant 0.07$ mm, we have $Oh_a \leqslant 5 \times 10^{-4}$, and so require $\Omega \gg 0.035$. This condition is satisfied in our experiments except for the smallest drops at the lowest frequencies. We proceed by neglecting the air drag, but bear in mind that, for $\Omega < 0.2$, its influence may become significant.

Note that, because (3.1) is linear, the coefficient of restitution C_R and contact time τ_C should be independent of the impact speed $X_\tau(0) = We^{1/2}$. This independence has been observed experimentally for liquid drops impacting a soap film (Gilet & Bush 2009*b*), a rigid substrate (Richard & Quéré 2000; Richard, Clanet & Quéré 2002) and a liquid bath (Jayaratne & Mason 1964; Zou *et al.* 2011), but only when $We \geqslant 1$. For $We < 1$, C_R and τ_C increase with decreasing impact speed, albeit quite weakly, as has been demonstrated numerically by Foote (1975) and Gopinath & Koch (2001), and experimentally by Okumura *et al.* (2003) for the case of a drop impacting a rigid superhydrophobic surface.

In order to see the dependence of the dynamics on the Weber number in the liquid–liquid setting of interest, we have measured C_R and τ_C for silicone oil drops of viscosity 20 and 50 cSt. The contact time was determined as the interval between the time when the bath beneath the drop first deforms and when the drop visibly detaches from the bath. The time of detachment is relatively difficult to pinpoint, owing to the small relative speed of the drop and underlying bath at that time. The measurement error was thus typically larger than the time difference of successive video frames. In order to determine C_R, we fitted the drop motion before and after the contact to parabolic trajectories, allowing us to calculate the instantaneous drop speed at both impact and detachment. With decreasing *We*, the amplitudes of the drop motion and bath deformation decrease, leading to a larger relative error in measurement of C_R and τ_C.

The results are shown in figures 10 and 11. We observe a logarithmic decrease of both contact time and coefficient of restitution with increasing Weber number, in line with the numerical predictions of Gopinath & Koch (2001). For small drops with $We > 1$, the coefficient of restitution tends to a value of $\sim$0.11 for 50 cSt oil

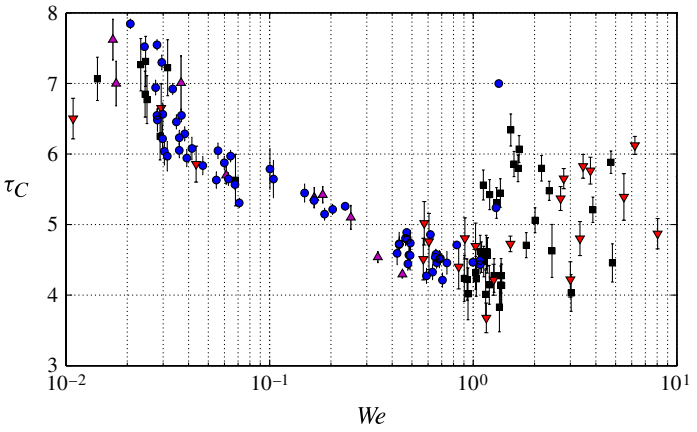

FIGURE 11. (Colour online) Non-dimensionalized contact time $\tau_C = T_C/(\rho R_0^3/\sigma)^{1/2}$ of silicone oil droplets impacting a bath of the same liquid, as a function of the Weber number $We = \rho R_0 V_{in}^2/\sigma$. Shown are results for 20 cSt (■) and 50 cSt (▼) droplets impacting a quiescent bath, together with values measured from drops impacting a vibrating bath just above the bouncing threshold, for 20 cSt (●) and 50 cSt (▲), respectively.

and ∼0.19 for 20 cSt oil, which should be compared to the value 0.22 obtained by Jayaratne & Mason (1964) for water (1 cSt). Figure 11 indicates that there is not an appreciable difference in the contact time between the two oils, unlike for a linear spring, for which larger damping leads to a longer period. As the Weber number is decreased, the contact time increases progressively until the point (around $We \approx 0.03$) where gravity prevents drop detachment.

Within a single regime diagram (i.e. for a fixed driving frequency and oil viscosity), the Weber number changes significantly with drop size and bouncing mode, while generally remaining below 1 (the lower extreme being $We \approx 0.003$ for small drops in the $(1, 1)$ mode at $f = 200$ Hz; the upper extreme being $We \approx 2$ for large drops in the $(2, 1)^2$ mode at $f = 50$ Hz). It is not surprising that the linear spring model with constant (C_R, τ_C) does not compare favourably with the experiments, since one expects both C_R and τ_C to depend on We. For example, using constant values of C_R within the experimentally observed range, that is, $C_R < 0.22$ for 50 cSt oil and $C_R < 0.35$ for 20 cSt, leads to a poor match. Note that changing τ_C (or C) has the effect of stretching the threshold curves vertically, so by choosing $\tau_C \approx 4.5$ we can match the curvature of the threshold curves. Changing C_R (or D) leads mainly to horizontal translation of the threshold curves on the regime diagram, so by picking the right value we can hope to fit one of the threshold curves. Figure 12 shows the results of the model with $C_R = 0.32$ (for $\nu = 50$ cSt) and $C_R = 0.42$ (for $\nu = 20$ cSt). We note that the upper parts of the other threshold curves are also well fitted by the model, presumably due to the fact that those parts of the regime diagram are already in the $We \geqslant 1$ regime, which is nearly linear. Nevertheless, the match for $\Omega < 0.4$ is less satisfactory, and the values of C_R are unrealistic when compared to those reported in figure 10.

A closer examination of the reaction force acting on the drop during rebound (see figure 21) provides a rationale for the unrealistically high values of C_R required to best fit the data with our linear spring model. During the late stages of contact, the viscous damping term dominates the spring term in (3.1) and the reaction force acting on the droplet pulls it towards the bath, a clearly unphysical effect if one neglects the

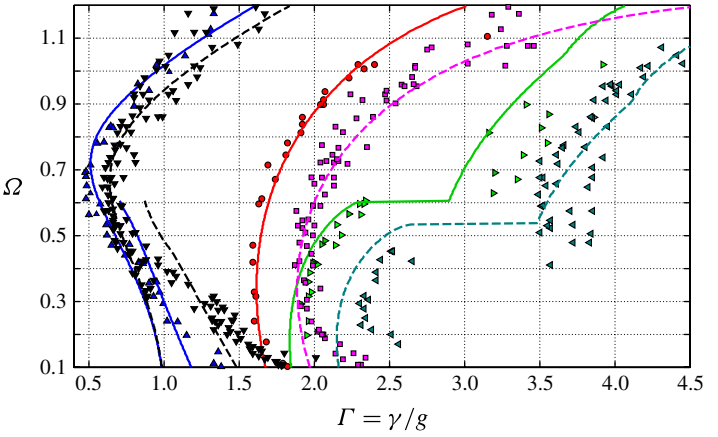

FIGURE 12. (Colour online) Comparison of the bouncing thresholds and the first two period-doubling transitions measured experimentally and calculated using the linear spring model (3.1). Refer to figure 3 to see where these transitions fit into the regime diagram. The linear model predictions with $C_R = 0.42$ and $\tau_C = 4.2$ (solid lines) are compared to experiments with 20 cSt oil in which coalescence (▲), first period doubling (●) and second period doubling (►) were measured. The predictions of the model with $C_R = 0.32$ and $\tau_C = 4.4$ (dashed lines) are compared to experiments with 50 cSt oil in which coalescence (▼), first period doubling (■) and second period doubling (◄) were measured. The lines shown are, from the left, the bouncing thresholds, $(1,1)^1 \leftarrow (1,1)^2$ mode transitions, first period-doubling $(1,1) \rightarrow (2,2)$ and second period-doubling $(2,2) \rightarrow (4,4)$ or $(2,1) \rightarrow (4,2)$.

intervening air layer dynamics. Therefore, a better model would be one in which the reaction force acting on the drop is always non-negative:

$$\frac{\partial^2 Z}{\partial \tau^2} = -Bo^*(\tau) + H(-Z)\max\left\{-D\frac{\partial Z}{\partial \tau} - CZ,\ 0\right\}. \tag{3.6}$$

With such a condition, the best match with the experimental data is indeed achieved with realistic values of C_R (specifically $C_R = 0.3$ for 20 cSt oil, and $C_R = 0.19$ for 50 cSt oil), but now the threshold curves in the regime diagrams are matched less well (see figure 13), especially the bouncing threshold. This shortcoming strongly suggests a Weber number dependence of C_R.

While the linear spring models presented in (3.1) and (3.6) do not provide satisfactory quantitative agreement with the experiments, and so will be superseded by an improved model to be developed in § 3.2, they have one major advantage. Specifically, the simple form of the equation of motion for the drop (3.1) allows one to obtain an analytic expression for the drop motion during both flight and contact. It is thus only necessary to obtain numerically the points of first impact and detachment; the motion in between can then be calculated with great speed, which makes it possible to obtain qualitatively correct regime diagrams with great resolution. One such regime diagram is shown in figure 14, obtained by choosing $C_R = 0.42$ and $\tau_C = 4.2$ in (3.1). The predicted bouncing thresholds shown in figures 12–14 correspond to the highest driving acceleration for which the drop never detaches from the bath surface (so that $Z(\tau) \leqslant 0$ always).

As mentioned previously, there can be several kinds of vertical motion corresponding to the same bouncing mode number (m, n), which can be thought of

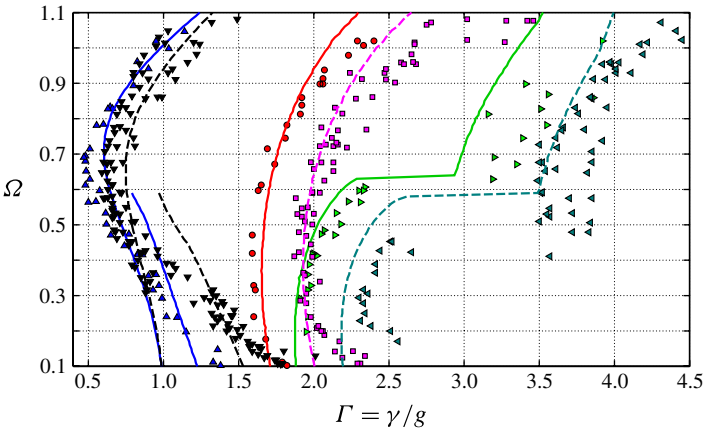

FIGURE 13. (Colour online) Comparison of the same experimental data as in figure 12 and the predictions of the second linear spring model (3.6) with $C_R = 0.3$ and $\tau_C = 4.2$ (solid lines), and with $C_R = 0.19$ and $\tau_C = 4.4$ (dashed lines). The lines shown are, from the left, the bouncing thresholds, $(1, 1)^1 \leftarrow (1, 1)^2$ mode transitions, first period-doubling $(1, 1) \rightarrow (2, 2)$ and second period-doubling $(2, 2) \rightarrow (4, 4)$ or $(2, 1) \rightarrow (4, 2)$.

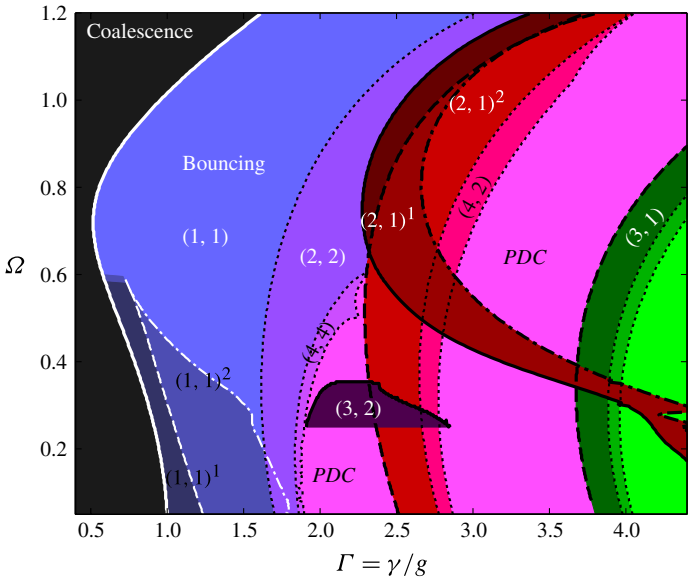

FIGURE 14. (Colour online) Regime diagram indicating the behaviour of a bouncing drop in the Γ–Ω plane, as predicted by the linear spring model (3.1) with $C_R = 0.42$ and $\tau_C = 4.2$. Here $\Omega = \omega/\omega_D$ is the vibration number and $\Gamma = \gamma/g$ is the dimensionless driving acceleration. In the (m, n) mode, the drop's motion has period equal to m driving periods, during which the drop hits the bath n times. *PDC* indicates a region of period-doubling cascade and chaos. Solid lines indicate lower boundaries of existence (or stability) of lower-energy modes, and dash-dotted lines indicate upper boundaries. Similarly, dashed lines indicate lower boundaries of existence of higher-energy modes, their upper boundaries being period-doubling transitions marked by dotted lines.

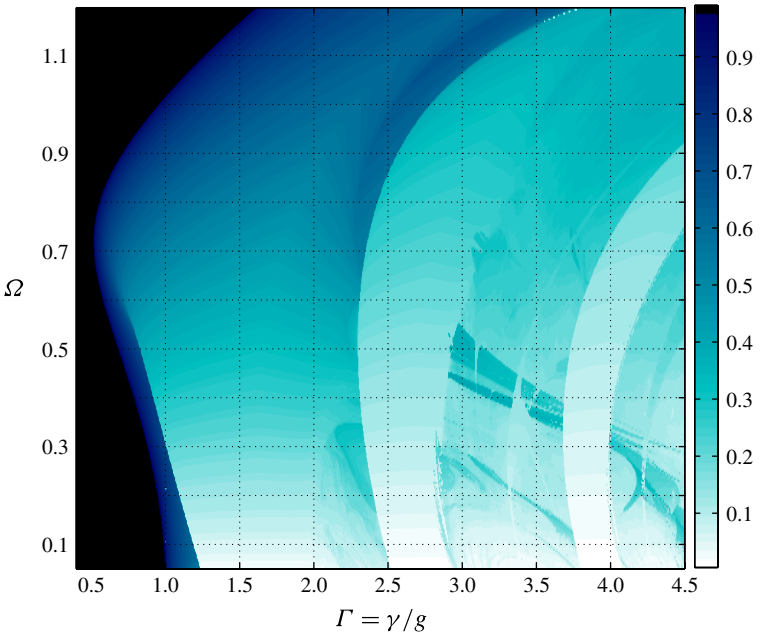

FIGURE 15. (Colour online) The relative contact time (fraction of the bouncing period spent in contact with the bath) of a bouncing drop in the Γ–Ω plane, as predicted by the linear spring model (3.1) with $C_R = 0.42$ and $\tau_C = 4.2$. Here Ω is the vibration number and Γ is the dimensionless driving acceleration. Sharp changes of the relative contact time are evident near $\Gamma \approx 1$ (the bouncing to oscillating transition, or the $(1,1)^2 \rightarrow (1,1)^1$ mode transition), $\Gamma \approx 2.4$ (onset of the $(2,1)^2$ mode) and $\Gamma \approx 3.7$ (onset of the $(3,1)$ mode).

as different energy levels. The lowest-energy mode tends to be the one where the drop spends the most time in contact with the bath. When average mechanical energy is increased, the drop spends more time in the air and less in contact with the bath. Figure 15 depicts the relative contact time as predicted by the linear spring model (3.1), for the highest-energy stable mode. We see two sharp transitions. The first arises for small drops ($\Omega < 0.55$), when the higher-energy $(1,1)^2$ bouncing mode can no longer be sustained and collapses to the least energetic vibrating mode $(1,1)^1$, in which the drop oscillates on the bath surface with a large portion of the period spent in contact with the bath. The second arises for larger drops ($\Omega > 0.6$), when the higher-energy $(2,1)^2$ mode cannot be sustained and only the base energy mode $(2,1)^1$ exists. Both of these transitions are prominent in our regime diagrams (figures 3–8): the former constitutes the lower part of the bouncing threshold, while the latter constitutes the upper half of the walking threshold, as will be seen in MBII.

In figures 16–18 we show the two different $(1,1)$ modes, the two $(2,1)$ modes and the $(3,2)$ bouncing mode, respectively. The dimensionless height of the drop in the laboratory frame of reference (solid line) and the equilibrium height of the vibrating bath (dashed line) are shown as functions of dimensionless time $\tau = ft$. In order to highlight the difference between the vibrating and bouncing states, the periods of contact between the drop and the bath are marked by a darker shading. In the vibrating state (figures 16*a* and 17*a*) the contact lasts roughly half the period of the drop's vertical motion, whereas in the bouncing state (figures 16*b* and 17*b*) the contact is

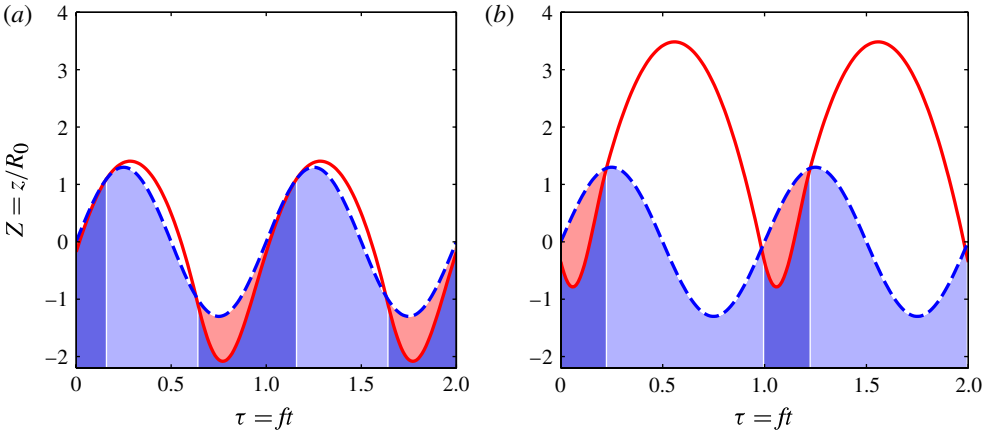

FIGURE 16. (Colour online) Comparison of (*a*) the low-energy 'vibrating' $(1, 1)^1$ mode and (*b*) the high-energy 'bouncing' $(1, 1)^2$ mode, as predicted by the linear spring model (3.1) with $\tau_C = 4.2$ and $C_R = 0.42$ for $(\Gamma, \Omega) = (1.3, 0.35)$. The dimensionless vertical position of the oscillating bath (dashed line) and the droplet's centre of mass shifted down by one radius (solid line) are shown as functions of the dimensionless time $\tau = ft$, where f is the bath's driving frequency. See figure 4(*a*,*b*) for the experimental realizations of these modes.

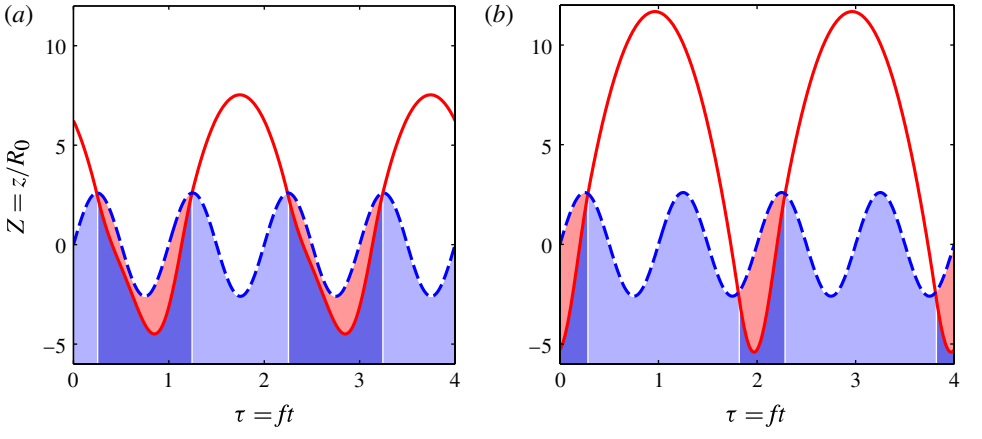

FIGURE 17. (Colour online) Comparison of (*a*) the lower-energy $(2, 1)^1$ mode and (*b*) the higher-energy $(2, 1)^2$ mode, as predicted by the linear spring model (3.1) with $\tau_C = 4.2$ and $C_R = 0.42$ for $(\Gamma, \Omega) = (2.6, 0.7)$. The dimensionless vertical position of the oscillating bath (dashed line) and the droplet's centre of mass shifted down by one radius (solid line) are shown as functions of the dimensionless time $\tau = ft$. See figure 4(*d*,*e*) for the experimental realizations of these modes.

significantly shorter. The $(3, 2)$ mode shown in figure 18 consists of one long and one short contact.

3.2. *Logarithmic spring model*

We have seen that the coefficient of restitution and the contact time of a drop interacting with a quiescent liquid bath are independent of the Weber number for $We > 1$, while for $We \leqslant 1$ they depend logarithmically on We (see figures 10 and 11).

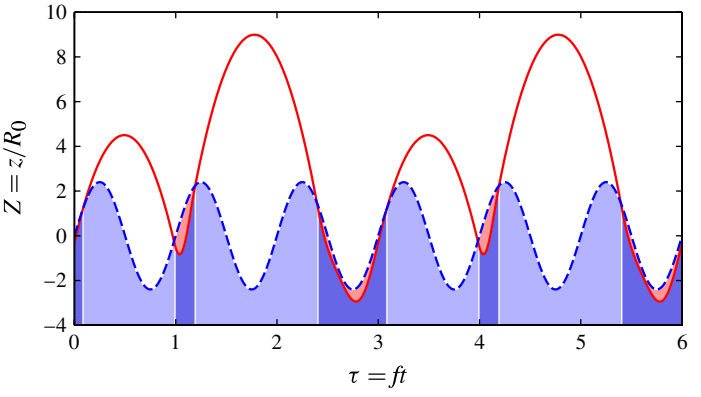

FIGURE 18. (Colour online) The (3, 2) mode, as predicted by the linear spring model (3.1) with $\tau_C = 4.2$ and $C_R = 0.42$ for $(\Gamma, \Omega) = (2.4, 0.32)$. The dimensionless vertical position of the oscillating bath (dashed line) and the droplet's centre of mass shifted down by one radius (solid line) are shown as functions of the dimensionless time $\tau = ft$.

Therefore, while in the former regime we can model the drop by a linear spring, in the latter we need a nonlinear model in order to capture, above all, the dependence of C_R on We. We derive such a model in the Appendix, using a quasi-static approximation similar to that developed previously for drop impact on a rigid substrate (Moláček & Bush 2012). The key idea of the resulting 'quasi-static' model is the approximation of the actual instantaneous shape of the drop and the bath by relatively simple shapes, specifically their quasi-static forms, which may be characterized by a small number of variables. By calculating the Lagrangian of the system, we can then derive the system of equations of motion for these variables. We then simplify the system to a single differential equation (A 14):

$$\frac{\mathrm{d}^2 Z}{\mathrm{d}\tau^2}\left(1 + \frac{c_3}{Q^2(Z)}\right) + Oh\frac{c_2(\nu)}{Q(Z)}\frac{\mathrm{d}Z}{\mathrm{d}\tau} + \frac{3/2}{Q(Z)}Z = -Bo^*(\tau), \tag{3.7}$$

where $Q(Z) = \ln(c_1/|Z|)$. Here c_3 prescribes the kinetic energy associated with the fluid motion within the two liquid bodies, $c_2(\nu)$ the amount of viscous dissipation within them, and c_1 the nonlinearity of the spring. For higher values of c_1, $\ln(c_1/|Z|)$ is less dependent on Z, thus making the spring more linear. The constants c_i are determined from matching to the observed dependence of the normal coefficient of restitution C_R on We (figure 10). The best match found is shown in figure 19, which was obtained by solving (A 13) for $R_0 = 0.15$ mm and two viscosities ($\nu = 20$ and 50 cSt), with the initial conditions $Z(0) = 0$ and $\mathrm{d}Z/\mathrm{d}\tau = -We$. The constants used were $c_2 = 12.5$ for 20 cSt and $c_2 = 7.5$ for 50 cSt, and $c_1 = 2$ and $c_3 = 1.4$ were used for both viscosities. Changing c_1 alters the slope of the line in figure 19, while changing c_2 shifts the line vertically. The fits were found to be quite insensitive to the value of c_3, suggesting that the internal fluid motion does not play a significant role in the impact dynamics, which is consistent with the scaling argument presented in Moláček & Bush (2012). In figure 20, the model predictions for the temporal evolution of the penetration depth are compared to the experimental data for $0.68 \leqslant We \leqslant 0.96$. Clearly, the linear spring model (3.1) overestimates C_R, and both linear models (3.1) and (3.6) underestimate the time elapsed until $|Z| = 0$, the drop's 'rebound time'. Note that the actual dimensionless contact time for $We \approx 0.8$ is approximately 4.3,

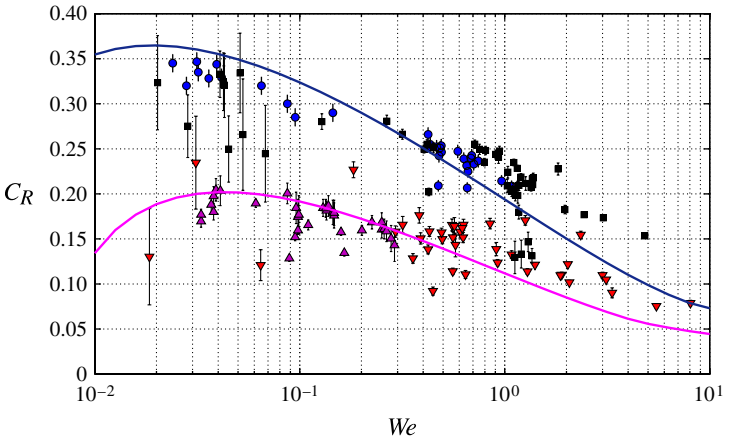

FIGURE 19. (Colour online) The dependence of the normal coefficient of restitution $C_R = V_{out}/V_{in}$ for silicone oil droplets impacting a bath of the same liquid, on the Weber number $We = \rho R_0 V_{in}^2/\sigma$. Shown are the experimental results for 20 cSt (■) and 50 cSt (▼) droplets impacting a quiescent bath. Analogous C_R values for droplets impacting a vibrating bath just above the bouncing threshold are also shown, for 20 cSt (●) and 50 cSt (▲), respectively. Solid lines indicate the values obtained using the logarithmic spring model (A 13) with $R_0 = 0.15$ mm for $c_1 = 2$, $c_2(20\text{ cSt}) = 12.5$, $c_2(50\text{ cSt}) = 7.5$ and $c_3 = 1.4$.

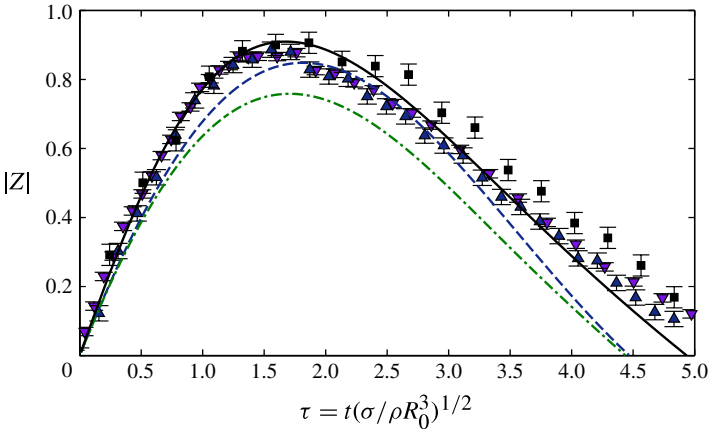

FIGURE 20. (Colour online) The dimensionless depth of penetration $|Z| = |z|/R_0 We^{1/2}$ of the drop's centre of mass below its height at the outset of contact (see figure 9), as a function of the dimensionless time $\tau = t(\sigma/\rho R_0^3)^{1/2}$. The predictions of the linear spring model (3.1) (dashed line), alternative linear spring model (3.6) (dash-dotted line) and the logarithmic spring model (3.7) (solid line) for $R_0 = 0.3$ mm and $We = 0.8$ are compared to the experimental values for $R_0 = 0.14$ mm, $We = 0.73$ (■), $R_0 = 0.20$ mm, $We = 0.68$ (▲) and $R_0 = 0.33$ mm, $We = 0.96$ (▼).

as the drop detaches while the bath is still deformed. In figure 21, we compare the predictions of the three models for the evolution of the dimensionless drop acceleration during contact. The linear models produce substantially different curves from the logarithmic model, predicting a significant acceleration immediately after

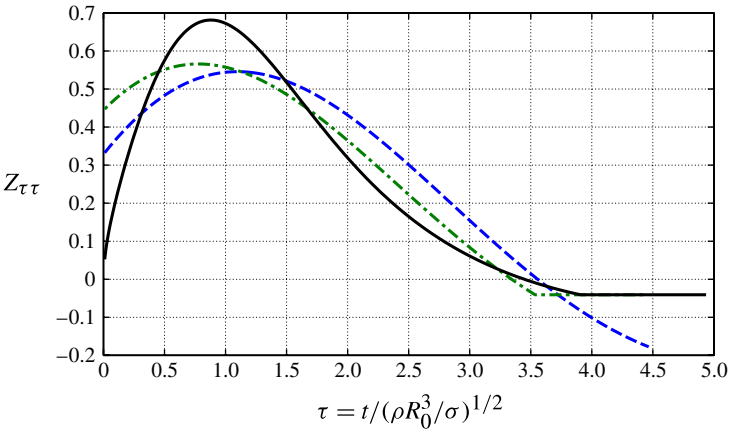

FIGURE 21. (Colour online) The dimensionless acceleration $Z_{\tau\tau} = (\mathrm{d}^2z/\mathrm{d}t^2)(\rho R_0^3/\sigma V_{in}^2)^{1/2}$ of the drop's centre of mass as a function of the dimensionless time $\tau = t(\sigma/\rho R_0^3)^{1/2}$. The predictions of the linear spring model (3.1) (dashed line), alternative linear spring model (3.6) (dash-dotted line) and the logarithmic spring model (3.7) (solid line) are shown for $R_0 = 0.3$ mm and $We = 0.8$.

impact and a stronger reaction force during the later stages of contact. The first linear model (3.1) also shows an unphysical negative reaction force during the late stages of contact, as indicated by the dip below the gravitational acceleration for $\tau > 3.8$.

Using the same combination of constants c_i as in figure 19, the regime diagram predicted using the logarithmic spring model (3.7) matches well with the experimental data (figure 22). Specifically, the lower part of the experimentally observed bouncing threshold curve now corresponds to the $(1, 1)^1 \leftarrow (1, 1)^2$ mode transition, which was not the case for the previous models. The mode transition (2, 1)–(4, 2) for 20 cSt (upper right corner of figure 22*a*,*b*) is matched least well; however, the match is still better than that produced by either of the linear models. Note that we had no freedom in choosing the curvature (vertical scale) of the threshold curves in figure 22 unlike the previous cases (figures 12 and 13), where it was determined by the parameter τ_C (or spring constant C). In the logarithmic spring model (3.7), the spring constant is $1.5/Q(Z)$ and therefore, apart from the weak nonlinear contribution from $Q(Z)$, is determined from the low-Weber-number analysis. The fact that the curvature and peaks of the predicted threshold curves correspond to those measured experimentally provides additional verification of our model.

A useful way to characterize the drop's impact in relation to the bath vibration is provided by the *impact phase* relative to the driving, defined as the weighted average of the driving phase $\Omega\tau$ over the contact time:

$$\Phi = \int_{\tau_C} F(\tau)(\Omega\tau)\,\mathrm{d}\tau \Big/ \int_{\tau_C} F(\tau)\,\mathrm{d}\tau \pmod{2\pi}, \tag{3.8}$$

where $F(\tau) = \partial^2 Z/\partial\tau^2 + Bo^*(\tau) = Z_{\tau\tau}(\tau) + Bo(1 + \Gamma \sin\Omega\tau)$ is the dimensionless reaction force acting on the drop during contact. Thus, $\Phi = \pi$ corresponds to impact at maximum upward bath velocity, whereas $\Phi = 0$ corresponds to the impact at maximum downward bath velocity. The impact phase Φ divided by π is shown in figure 23 as a function of the driving acceleration $\Gamma = \gamma/g$ for three values of Ω,

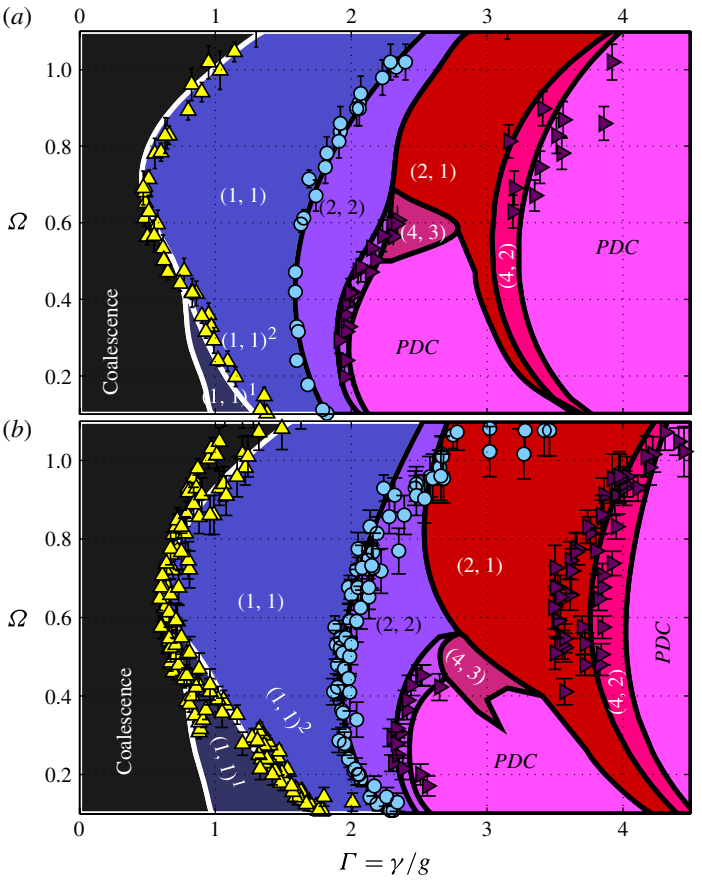

FIGURE 22. (Colour online) Comparison of the regime diagrams measured experimentally and those calculated using the logarithmic spring model (3.7). (*a*) The model predictions with $c_1 = 2$, $c_3 = 1.4$, $c_2 = 12.5$ and $f = 80$ Hz (solid lines) are compared to experiments with 20 cSt oil in which coalescence (▲), first period doubling (●) and second period doubling (►) were measured. (*b*) The predictions of the model with $c_1 = 2$, $c_3 = 1.4$, $c_2 = 7.5$ and $f = 80$ Hz (dashed lines) are compared to experiments with 50 cSt oil in which coalescence (▲), first period doubling (●) and second period doubling (►) were measured.

specifically $\Omega = 0.2$, 0.5 and 0.8. The results were obtained using the model (3.7) with $c_1 = 2$, $c_3 = 1.4$, $c_2 = 7.5$ and $f = 80$ Hz. The weighted average of Φ/π is indicated by dark lines and dots, while the extent of contact is marked by shaded regions, with lighter shading indicating that the droplet is in contact during the corresponding phase only on a small number of impacts per its period of motion.

For $\Omega = 0.8$ (figure 23*c*), the drop coalesces with the bath when $\Gamma < 0.49$. As the driving is increased above this value, the drop begins to detach from the surface (white regions), and the contact time decreases, as indicated by the vertical extent of the shaded region. The impact phase slowly increases from approximately π at $\Gamma = 0.5$ to 1.2π at $\Gamma = 1.9$, where the first period doubling occurs. There, the even and odd contacts separate, with the impact phase of one increasing and of the other decreasing. At $\Gamma \approx 2.3$, one of the ends of contact joins with the beginning of the following contact, and the completely period-doubled $(2, 1)^1$ mode is formed (note the discrete

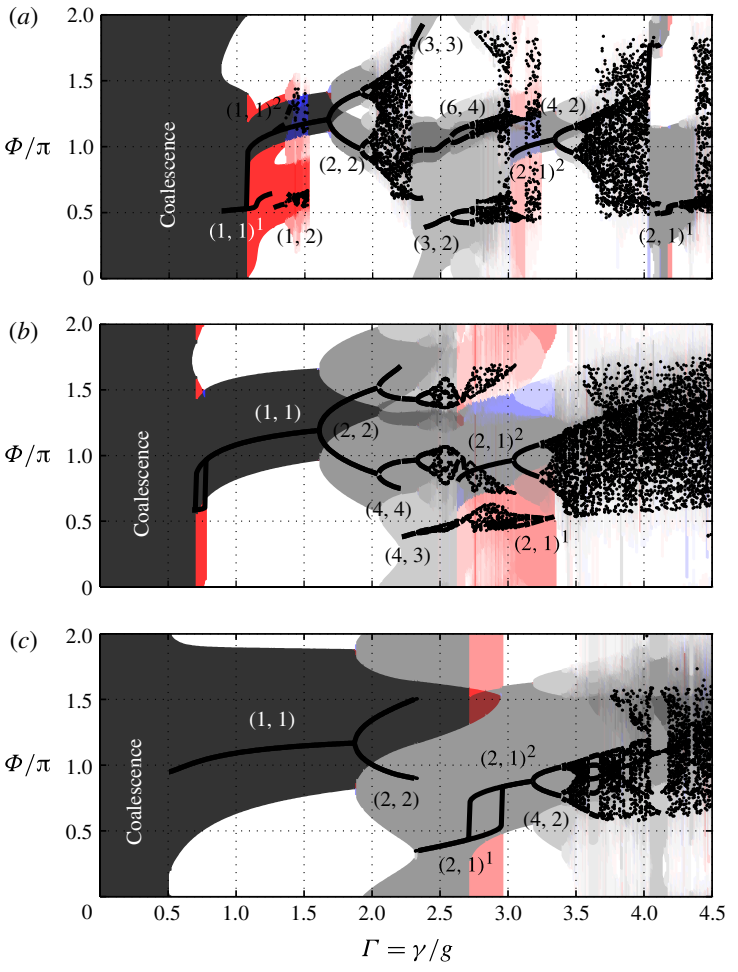

FIGURE 23. (Colour online) The dependence of the impact phase Φ (solid lines, points), defined in (3.8), on the driving acceleration $\Gamma = \gamma/g$ for three values of the vibration number Ω: (*a*) $\Omega = 0.2$, (*b*) $\Omega = 0.5$ and (*c*) $\Omega = 0.8$ (refer to figure 22*a*). Contact is marked by the shaded regions, wherein the darkness of the shading indicates the relative number of contacts including the given phase. Where possible, the periodic bouncing modes (m, n) are indicated.

change of impact phase by π). Increasing the driving to $\Gamma \approx 2.95$, the $(2, 1)^1$ vibrating mode becomes unstable to the $(2, 1)^2$ bouncing mode, with markedly shorter contact time. Once in this mode, we can decrease the driving acceleration to $\Gamma \approx 2.7$ before we switch back to the $(2, 1)^1$ mode. Further increase of Γ beyond $\Gamma = 3$ leads to a period-doubling cascade and the onset of chaos at $\Gamma \approx 3.45$.

The most common bouncing modes are labelled in figure 23, where we observe that the impact phase is higher for higher-energy (bouncing) states than for their lower-energy counterparts, with the higher-energy state disappearing once the phase dips below π. This disappearance can be rationalized by considering the vertical bath speed in an inertial frame of reference, given by $-(Bo/\Omega)\cos(\Omega\tau)$, which achieves its maximum value when $\Phi = \pi$. Thus, when $\Phi = \pi$, the bath transfers the maximum momentum possible to the drop during contact; below this value the drop

cannot maintain the higher energy level and collapses to a lower-energy bouncing mode. We note that, with increasing vibration number Ω (or, equivalently, increasing drop size), the duration of contact increases, chaotic bouncing states are replaced by periodic states, and the lower-energy modes $(1, 1)^1$ and $(2, 1)^1$ shift to lower driving accelerations.

4. Discussion

In our experiments, we have classified the drop dynamics for a wide range of driving frequencies and drop sizes, and reported a number of new bouncing states. We have reported the full bouncing threshold curve and shown that it can be discontinuous. We observed the existence of two distinct bouncing states corresponding to the same mode number (m, n), which we dubbed 'bouncing' and 'vibrating'. The transition between these two energy levels of the same mode plays a crucial role in the coalescence of small drops and in the onset of walking for larger drops. For small drops, the contact time in the $(1, 1)^1$ mode, being roughly half the oscillation period, is longer than the thinning time of the intervening air layer, resulting in coalescence. The lower part of the bouncing threshold curve therefore lies along the $(1, 1)^1$–$(1, 1)^2$ transition curve. The peak of the walking region typically occurs on the transition curve between the $(2, 1)^1$ and the $(2, 1)^2$ modes, as will be shown in MBII. The dominance of the $(2, 1)^2$ mode beyond this point is responsible for the walking region having only finite extent.

We have thus delineated the different regimes arising in the vertical dynamics of a drop bouncing on a vibrating bath and rationalized them using a logarithmic spring model for the drop–bath interaction. For small driving accelerations, the bath cannot transfer energy to the drop at a rate sufficient to compensate for viscous dissipation and wave creation; consequently, the drop coalesces when the intervening air layer thins below a critical thickness. For higher driving accelerations, simple periodic bouncing is observed, which tends to become unstable to more complex bouncing states with longer period, as the driving amplitude is further increased. Generally, as the driving acceleration is raised, the average contact time of the drop decreases and the amplitude of its bounce increases, but the change between bouncing modes is sometimes discrete. For even higher accelerations, chaotic bouncing is the norm, interspersed with windows of periodicity. Nevertheless, the chaotic regions disappear for larger drops and near the Faraday threshold, where the standing-wave pattern created by the drop's impacts acts to stabilize the vertical motion by reducing the relative speed of the drop and bath at impact.

We have developed a series of models of increasing sophistication to describe the dynamics of drops bouncing on a vibrating fluid bath. The dynamics involve a complex interplay of the drop and bath deformation and also of the air flow in the intervening layer during contact. However, provided there is no coalescence, the air film between the drop and the bath serves only to communicate normal stresses between the two. We have shown that, in the parameter regime of interest, many factors can be neglected, such as the role of air drag during flight and the residual bath deformation generated by previous drop impacts. This allowed us to simplify the dynamics to the point that it could be captured by a single differential equation, with the reaction force acting during contact modelled as a linear or logarithmic spring. The linear spring model, which has been used previously to model drop rebound from a rigid substrate (Okumura *et al.* 2003), has two free parameters, the spring

and dissipation constants, which can be determined experimentally by measuring the contact time T_C and coefficient of restitution C_R.

The linear spring models, by virtue of their linearity, were unable to correctly model the dependence of C_R on the impact speed. Nevertheless, their integrability allows fast numerical solution, which might make them preferable in some cases where speed takes precedence over accuracy. The logarithmic spring model is new, derived by analysis of the dynamics at very small Weber numbers and extension to the parameter regime of interest. It has three free parameters, which can be determined by measuring T_C and C_R for two different impact speeds. Only the logarithmic spring model was found to be consistent with the experimental data for Weber numbers smaller than 1. Even the bouncing threshold, which in general requires understanding of the intervening layer dynamics, could be almost entirely rationalized by considering mode transitions and contact time. For applications requiring a highly accurate representation of the temporal dependence of the reaction force, as will be the case for the model of walking drops treated in our subsequent paper (MBII), the logarithmic spring model will be invaluable.

Throughout our analysis, we have assumed that both the drop and bath deformations are dissipated between impacts, an assumption that breaks down as one approaches the Faraday threshold. Then, the purely vertical bouncing states can be destabilized by the standing waves, giving rise to walking states, an effect to be treated in MBII. There, we couple the drop's vertical dynamics, as described herein, to its horizontal dynamics. In order to determine the amplitude of the standing waves created and the tangential acceleration they impart to the drop, it is necessary to know the impact phase and the temporal dependence of the reaction force. The model for the vertical dynamics developed herein provides this information, the absence of which is responsible for the shortcomings of previous theoretical descriptions (Couder *et al.* 2005*b*; Eddi *et al.* 2011*b*) of this relatively subtle system.

Acknowledgements

The authors thank the National Science Foundation for their generous financial support through grant CBET-0966452, and the MIT–France Program. We also thank D. Harris for his indispensable help with the experiments and Y. Couder and his group for valuable discussions.

Appendix. Derivation of the logarithmic spring equation

We consider the regime $We \ll 1$ and build a quasi-static model similar to that developed for drop impact on a rigid substrate (Moláček & Bush 2012). The actual instantaneous shapes of the drop and the bath are approximated by relatively simple shapes characterized by a small number of variables. The family of shapes we choose is one consisting of sessile shapes of liquid drops resting on a liquid bath (now not necessarily made of the same liquid as the drop). The reason for this choice is that, in the $We \ll 1$ regime, when the overall rebound dynamics is slow relative to the dynamics of the typical surface waves created, one expects the surface shapes to equilibrate to some quasi-static form (Bach, Koch & Gopinath 2004). If the drop has surface tension σ_D and density ρ_D, and the bath σ_B and ρ_B, the sessile shape family has dimensionality three by Buckingham's theorem; it can be parametrized by two Bond numbers $A = Bo_D = \rho_D g R_0^2/\sigma_D$ and $C = Bo_B = \rho_B g R_0^2/\sigma_B$ and by the parameter $B = \sigma_D Bo_D/\sigma_B$. Although in our system we have $\sigma = \sigma_B$ and $\rho = \rho_B$, initially we keep these variables separate in order to describe the deformation of the drop and bath

independently. Parameter A prescribes the magnitude of the drop's deformation, B the vertical bath deformation and C the horizontal extent of bath deformation. Minimizing the total potential energy of the drop and bath allows one to obtain the sessile profile of the drop–bath system and the corresponding values of the total surface and gravitational potential energy. Keeping A, B and C independent for the time being, while setting $\sigma_D = \sigma_B = \sigma$ and $\rho_D = \rho_B = \rho$ for the sake of simplicity, we obtain

$$\frac{\mathscr{S}\mathscr{E}_{TOT}}{\pi\sigma R_0^2} \approx \frac{2}{9}A^2\left(\ln\frac{6}{(A+B)C} - 2\gamma - \frac{1}{2}\right) + \frac{2}{9}B^2\left(\ln\frac{6}{A+B} - \frac{4}{3}\right), \tag{A 1a}$$

$$\frac{\mathscr{P}\mathscr{E}_{TOT}}{\pi\sigma R_0^2 Bo} \approx -\frac{4}{9}A\left(\ln\frac{6}{(A+B)C} - 2\gamma + 1\right) - \frac{4}{9}B\left(\ln\frac{6}{A+B} - \frac{5}{6}\right) + \frac{2}{9}\frac{A^2}{C}. \tag{A 1b}$$

Here $\gamma = 0.577\,216\ldots$ is the Euler–Mascheroni constant, arising via a small-argument approximation of the Bessel function $\mathrm{K}_0(x)$. When the fluid viscosity is sufficiently low ($Oh \ll 1$), the flow inside the drop and bath can be approximated by a potential flow. Note that, in our experiments, $0.1 < Oh < 1$. Expressing the drop deformation as a sum of spherical harmonic modes, one can then evaluate the kinetic energy associated with a continuous change of drop shape within the sessile shape family (i.e. when $A = A(t)$). The kinetic energy of the bath, moving as a result of time-dependent parameters B and C, can be similarly obtained using the Hankel transform of the bath surface deformation. The total kinetic energy of the system is then given by

$$\frac{\mathscr{K}\mathscr{E}_{TOT}}{\pi\rho R_0^5} \approx \frac{\pi A^2}{C^{3/2}}\left[\frac{1}{9}\left(\frac{\dot{A}}{A}\right)^2 - \frac{1}{6}\left(\frac{\dot{A}}{A}\right)\left(\frac{\dot{C}}{C}\right) + \frac{5}{72}\left(\frac{\dot{C}}{C}\right)^2\right] + \frac{2}{9}C_{K0}\dot{B}^2 + \frac{2}{3}\dot{Z}^2, \tag{A 2}$$

where

$$Z = -\frac{A}{3}\left(\ln\frac{6}{(A+B)C} - 2\gamma\right) - \frac{B}{3}\left(\ln\frac{6}{A+B} - \frac{5}{6}\right) \leqslant 0 \tag{A 3}$$

is the dimensionless height of the drop's centre of mass ($Z = z/R_0$) and $C_{K0} = \pi^2/12 - 17/27 \approx 0.193$. The coordinates are chosen such that $Z = 0$ when the drop is spherical and the bath flat ($A = B = 0$, corresponding to the initiation of impact). The viscous dissipation inside the drop and bath can also be calculated using the potential flow approximation, provided the condition $Oh \ll 1$ is satisfied. Doing so yields

$$\frac{\mathscr{D}_{TOT}}{\pi\mu R_0^3} = \frac{2\pi A^2}{C^{1/2}}\left[\frac{4}{9}\left(\frac{\dot{A}}{A}\right)^2 - \frac{2}{9}\left(\frac{\dot{A}}{A}\right)\left(\frac{\dot{C}}{C}\right) + \frac{1}{18}\left(\frac{\dot{C}}{C}\right)^2\right] + \frac{8}{9}C_{D0}\dot{B}^2, \tag{A 4}$$

where $C_{D0} = \pi^2/4 - 5/12 \approx 2.051$. For a more detailed derivation of (A 3) and (A 4), see Moláček & Bush (2012). Using expressions (A 1)–(A 4), the equations of motion can be derived using the Euler–Langrange equation with dissipation (see Torby 1984):

$$\frac{\mathrm{d}}{\mathrm{d}t}\left[\frac{\partial\mathfrak{L}}{\partial\dot{X}}\right] + \frac{1}{2}\frac{\partial\mathscr{D}_{TOT}}{\partial\dot{X}} = \frac{\partial\mathfrak{L}}{\partial X}, \tag{A 5}$$

where the Lagrangian $\mathfrak{L} = \mathscr{K}\mathscr{E}_{TOT} - \mathscr{S}\mathscr{E}_{TOT} - \mathscr{P}\mathscr{E}_{TOT}$. It should be stressed that the expressions (A 1)–(A 4) are only leading-order approximations valid in the limit of small deformations (i.e. when $A, B, C \ll 1$), which arises for impacts at small We.

In order to avoid dealing with a system of three differential equations with three variables, we need to further simplify the model. Since the drop and bath

consist of the same liquid, we expect their deformation to be similar in magnitude (i.e. $A(t) \approx B(t)$), which can be verified either experimentally or by solving the full 3×3 system. Therefore, we set $A = B$. In the moderate-Weber-number regime ($0.01 < We \lesssim 1$), deformation of the bath occurs predominantly in the region near the drop. The horizontal length scale of significant bath deformation, though increasing in time, then remains comparable to the drop radius R_0 throughout the impact, suggesting that we approximate C by a constant. Doing so, we are left with a single independent variable $A(t)$. Thus (A 1)–(A 4) simplify to

$$\frac{\mathscr{S}\mathscr{E}_{TOT}}{\pi\sigma R_0^2} \approx \frac{2}{9}A^2\left(2\ln\frac{3}{A} - \ln C - 2\gamma - \frac{11}{6}\right), \quad \frac{\mathscr{P}\mathscr{E}_{TOT}}{\pi\sigma R_0^2 Bo} \approx \frac{4}{3}Z + \frac{2}{9}\frac{A^2}{C}, \tag{A 6}$$

$$\frac{\mathscr{K}\mathscr{E}_{TOT}}{\pi\rho R_0^5} \approx \frac{2}{3}\dot{Z}^2 + \frac{2}{9}C_{K0}\dot{A}^2 + \frac{\pi}{9}\frac{\dot{A}^2}{C^{3/2}}, \qquad \frac{\mathscr{D}_{TOT}}{\pi\mu R_0^3} \approx \frac{8}{9}\frac{\pi\dot{A}^2}{C^{1/2}} + \frac{16}{9}C_{D0}\dot{A}^2, \tag{A 7}$$

with

$$Z = -\frac{A}{3}\left(2\ln\frac{3}{A} - \ln C - 2\gamma - \frac{5}{6}\right). \tag{A 8}$$

We now express (A 6) and (A 7) in terms of Z instead of A, employing the fact that, for small A, (A 8) can be rewritten as

$$A = -\frac{3Z}{2\ln(-1/Z) + \cdots}. \tag{A 9}$$

Assuming $|Z| \ll 1$ and keeping only the leading-order contributions in each expression, we obtain

$$\frac{\mathscr{S}\mathscr{E}_{TOT}}{\pi\sigma R_0^2} \approx \frac{Z^2}{\ln(\alpha/|Z|)}, \qquad \frac{\mathscr{P}\mathscr{E}_{TOT}}{\pi\sigma R_0^2 Bo} \approx \frac{4}{3}Z, \tag{A 10}$$

$$\frac{\mathscr{K}\mathscr{E}_{TOT}}{\pi\rho R_0^5} \approx \frac{2}{3}\dot{Z}^2 + \frac{(2C_{K0} + \pi C^{-3/2})\dot{Z}^2}{\ln^2(\alpha/|Z|)}, \quad \frac{\mathscr{D}_{TOT}}{\pi\mu R_0^3} \approx \frac{(16C_{D0} + 8\pi C^{-1/2})\dot{Z}^2}{\ln^2(\alpha/|Z|)}. \tag{A 11}$$

Switching to the dimensionless time $\tau = t/(\rho R_0^3/\sigma)^{1/2}$ and using (A 5), we derive the following equation of motion, keeping the leading-order terms only:

$$\frac{\mathrm{d}^2 Z}{\mathrm{d}\tau^2}\left[1 + \frac{3C_{K0} + 1.5\pi C^{-3/2}}{\ln^2(\alpha/|Z|)}\right] + Oh\frac{6\pi C^{-1/2} + 12C_{D0}}{\ln^2(\alpha/|Z|)}\frac{\mathrm{d}Z}{\mathrm{d}\tau} + \frac{3/2}{\ln(\alpha/|Z|)}Z = -Bo. \tag{A 12}$$

Equation (A 12) suggests that the impact of a drop on a quiescent bath can be approximated by a 'logarithmic spring' model of the form

$$\frac{\mathrm{d}^2 Z}{\mathrm{d}\tau^2}\left(1 + \frac{c_3}{\ln^2(c_1/|Z|)}\right) + Oh\frac{c_2(Oh)}{\ln^2(c_1/|Z|)}\frac{\mathrm{d}Z}{\mathrm{d}\tau} + \frac{3/2}{\ln(c_1/|Z|)}Z = -Bo, \tag{A 13}$$

where c_1, c_2 and c_3 are constants to be determined. Replacing Bo in (A 13) by the effective Bond number $Bo^*(\tau) = Bo(1 + \Gamma\sin\Omega\tau)$, we obtain the logarithmic spring model for a drop bouncing on a vibrating bath:

$$\frac{\mathrm{d}^2 Z}{\mathrm{d}\tau^2}\left(1 + \frac{c_3}{Q^2(Z)}\right) + Oh\frac{c_2(\nu)}{Q(Z)}\frac{\mathrm{d}Z}{\mathrm{d}\tau} + \frac{3/2}{Q(Z)}Z = -Bo^*(\tau), \tag{A 14}$$

where $Q(Z) = \ln(c_1/|Z|)$.

REFERENCES

BACH, G. A., KOCH, D. L. & GOPINATH, A. 2004 Coalescence and bouncing of small aerosol droplets. *J. Fluid Mech.* **518**, 157–185.

BENJAMIN, T. & URSELL, F. 1954 The stability of the plane free surface of a liquid in vertical periodic motion. *Proc. R. Soc. Lond.* A **225**, 505–515.

BUSH, J. W. M. 2010 Quantum mechanics writ large. *Proc. Natl. Acad. Sci.* **107**, 17 455–17 456.

CAI, Y. K. 1989 Phenomena of a liquid drop falling to a liquid surface. *Exp. Fluids* **7**, 388–394.

CHANDRASEKHAR, S. 1961 *Hydrodynamic and Hydromagnetic Stability*. Clarendon.

CHING, B., GOLAY, M. W. & JOHNSON, T. J. 1984 Droplet impacts upon liquid surfaces. *Science* **226**, 535–537.

COUDER, Y. & FORT, E. 2006 Single-particle diffraction and interference at macroscopic scale. *Phys. Rev. Lett.* **97**, 154101.

COUDER, Y., FORT, E., GAUTIER, C. H. & BOUDAOUD, A. 2005*a* From bouncing to floating: noncoalescence of drops on a fluid bath. *Phys. Rev. Lett.* **94**, 177801.

COUDER, Y., PROTIÈRE, S., FORT, E. & BOUDAOUD, A. 2005*b* Dynamical phenomena: walking and orbiting droplets. *Nature* **437**, 208.

DAVIS, R. B. & VIRGIN, L. N. 2007 Non-linear behaviour in a discretely forced oscillator. *Intl J. Non-Linear Mech.* **42**, 744–753.

EDDI, A., BOUDAOUD, A. & COUDER, Y. 2011*a* Oscillating instability in bouncing droplet crystals. *Europhys. Lett.* **94**, 20004.

EDDI, A., DECELLE, A., FORT, E. & COUDER, Y. 2009*a* Archimedean lattices in the bound states of wave interacting particles. *Europhys. Lett.* **87**, 56002.

EDDI, A., FORT, E., MOISY, F. & COUDER, Y. 2009*b* Unpredictable tunneling of a classical wave–particle association. *Phys. Rev. Lett.* **102**, 240401.

EDDI, A., MOUKHTAR, J., PERRARD, S., FORT, E. & COUDER, Y. 2012 Level splitting at macroscopic scale. *Phys. Rev. Lett.* **108**, 264503.

EDDI, A., SULTAN, E., MOUKHTAR, J., FORT, E., ROSSI, M. & COUDER, Y. 2011*b* Information stored in Faraday waves: the origin of a path memory. *J. Fluid Mech.* **674**, 433–463.

EDDI, A., TERWAGNE, D., FORT, E. & COUDER, Y. 2008 Wave propelled ratchets and drifting rafts. *Europhys. Lett.* **82**, 44001.

EICHWALD, B., ARGENTINA, M., NOBLIN, X. & CELESTINI, F. 2010 Dynamics of a ball bouncing on a vibrated elastic membrane. *Phys. Rev.* E **82**, 016203.

EVERSON, R. M. 1986 Chaotic dynamics of a bouncing ball. *Physica* D **19**, 355–383.

FARADAY, M. 1831 On a peculiar class of acoustical figures; and on certain forms assumed by groups of particles upon vibrating elastic surfaces. *Phil. Trans. R. Soc. Lond.* **121**, 299–340.

FERMI, E. 1949 On the origin of the cosmic radiation. *Phys. Rev.* **75**, 1169–1174.

FLEMMER, R. L. C. & BANKS, C. L. 1986 On the drag coefficient of a sphere. *Powder Technol.* **48**, 217–221.

FOOTE, G. B. 1975 The water drop rebound problem: dynamics of collision. *J. Atmos. Sci.* **32**, 390–402.

FORT, E., EDDI, A., BOUDAOUD, A., MOUKHTAR, J. & COUDER, Y. 2010 Path-memory induced quantization of classical orbits. *Proc. Natl. Acad. Sci.* **107**, 17 515–17 520.

GILET, T. & BUSH, J. W. M. 2009*a* Chaotic bouncing of a droplet on a soap film. *Phys. Rev. Lett.* **102**, 014501.

GILET, T. & BUSH, J. W. M. 2009*b* The fluid trampoline: droplets bouncing on a soap film. *J. Fluid Mech.* **625**, 167–203.

GOPINATH, A. & KOCH, D. L. 2001 Dynamics of droplet rebound from a weakly deformable gas–liquid interface. *Phys. Fluids* **13**, 3526–3532.

HALLETT, J. & CHRISTENSEN, L. 1984 Splash and penetration of drops in water. *J. Rech. Atmos.* **18**, 225–242.

HARRIS, D. M., MOUKHTAR, J., FORT, E., COUDER, Y. & BUSH, J. W. M. 2013 Wave-like statistics from pilot-wave dynamics in a circular corral. *Phys. Rev.* E (submitted).

HARTLAND, S. 1969 The effect of circulation patterns on the drainage of the film between a liquid drop and a deformable liquid–liquid interface. *Chem. Engng Sci.* **24**, 611–613.

HARTLAND, S. 1970 The profile of the draining film between a fluid drop and a deformable fluid–liquid interface. *Chem. Engng J.* **1**, 67–75.

JAYARATNE, O. W. & MASON, B. J. 1964 The coalescence and bouncing of water drops at an air/water interface. *Proc. R. Soc. Lond.* A **280**, 545–565.

JONES, A. F. & WILSON, S. D. R. 1978 The film drainage problem in droplet coalescence. *J. Fluid Mech.* **87**, 263–288.

KUMAR, K. 1996 Linear theory of Faraday instability in viscous liquids. *Proc. Math. Phys. Engng Sci.* **452**, 1113–1126.

LUCK, J. M. & MEHTA, A. 1993 Bouncing ball with a finite restitution: chattering, locking, and chaos. *Phys. Rev.* E **48**, 3988–3997.

LUNA-ACOSTA, G. A. 1990 Regular and chaotic dynamics of the damped Fermi accelerator. *Phys. Rev.* A **42**, 7155–7162.

MILLER, C. A. & SCRIVEN, L. E. 1968 The oscillations of a fluid droplet immersed in another fluid. *J. Fluid Mech.* **32**, 417–435.

MOLÁČEK, J. & BUSH, J. W. M. 2012 A quasi-static model of drop impact. *Phys. Fluids* **24**, 127103.

MOLÁČEK, J. & BUSH, J. W. M. 2013 Drops walking on a vibrating bath: towards a hydrodynamic pilot-wave theory. *J. Fluid Mech.* **727**, 612–647.

OKUMURA, K., CHEVY, F., RICHARD, D., QUÉRÉ, D. & CLANET, C. 2003 Water spring: a model for bouncing drops. *Europhys. Lett.* **62**, 237–243.

PIERANSKI, P. 1983 Jumping particle model. Period doubling cascade in an experimental system. *J. Phys. (Paris)* **44**, 573–578.

PIERANSKI, P. & BARTOLINO, R. 1985 Jumping particle model. Modulation modes and resonant response to a periodic perturbation. *J. Phys. (Paris)* **46**, 687–690.

PROSPERETTI, A. 1980 Free oscillations of drops and bubbles: the initial-value problem. *J. Fluid Mech.* **100**, 333–347.

PROSPERETTI, A. & OGUZ, H. N. 1993 The impact of drops on liquid surfaces and the underwater noise of rain. *Annu. Rev. Fluid Mech.* **25**, 577–602.

PROTIÈRE, S., BOHN, S. & COUDER, Y. 2008 Exotic orbits of two interacting wave sources. *Phys. Rev.* E **78**, 036204.

PROTIÈRE, S., BOUDAOUD, A. & COUDER, Y. 2006 Particle–wave association on a fluid interface. *J. Fluid Mech.* **554**, 85–108.

PROTIÈRE, S. & COUDER, Y. 2006 Orbital motion of bouncing drops. *Phys. Fluids* **18**, 091114.

PROTIÈRE, S., COUDER, Y., FORT, E. & BOUDAOUD, A. 2005 The self-organization of capillary wave sources. *J. Phys.: Condens. Matter* **17**, S3529–S3535.

RAYLEIGH, LORD 1879 On the capillary phenomena of jets. *Proc. R. Soc. Lond.* A **29**, 71.

RICHARD, D., CLANET, C. & QUÉRÉ, D. 2002 Surface phenomena: contact time of a bouncing drop. *Nature* **417**, 811.

RICHARD, D. & QUÉRÉ, D. 2000 Bouncing water drops. *Europhys. Lett.* **50**, 769–775.

SCHOTLAND, R. M. 1960 Experimental results relating to the coalescence of water drops with water surfaces. *Discuss. Faraday Soc.* **30**, 72–77.

TERWAGNE, D. 2011 Bouncing droplets, the role of deformations. PhD thesis, Université de Liège.

TERWAGNE, D., GILET, T., VANDEWALLE, N. & DORBOLO, S. 2008 From bouncing to boxing. *Chaos* **18**, 041104.

TERWAGNE, D., LUDEWIG, F., VANDEWALLE, N. & DORBOLO, S. 2013 The role of deformations in the bouncing droplet dynamics. *Phys. Fluids* (submitted) arXiv:1301.7463.

TORBY, B. J. 1984 *Advanced Dynamics for Engineers*. Holt, Rinehart and Winston.

WALKER, J. 1978 Drops of liquid can be made to float on the liquid. What enables them to do so? *The Amateur Scientist, Sci. Am.* **238**, 151–158.

ZOU, J., WANG, P. F., ZHANG, T. R., FU, X. & RUAN, X. 2011 Experimental study of a drop bouncing on a liquid surface. *Phys. Fluids* **23**, 044101.